Smart Structures and Systems, *Vol. 36, No. 3 (2025) 139-155*
https://doi.org/10.12989/sss.2025.36.3.139

Overhaul of nano-sensors through inventive head design and certified performance improvements using construction building information modeling

Haoxiang Guo [1], Gongxing Yan[*1], Sultan Saleh Alnahdi [2], Liang Yin[**3], Belgacem Bouallegue [4], Abdullah Alnutayfat [5], Rania M. Ghoniem [6], Hamid Assilzadeh[***7,8] and José Escorcia-Gutierrez [9]

[1] *School of Intelligent Construction, Luzhou Vocational and Technical College, Luzhou 646000, Sichuan, China*
[2] *Civil Engineering Department, College of Engineering, University of Business and Technology, Jeddah 21361, Saudi Arabia*
[3] *Department of Civil Engineering, Faculty of Engineering, University of Malaya, 50603, Kuala Lumpur, Malaysia*
[4] *Department of Computer Engineering, College of Computer Science, King Khalid University, ABHA, 61421, Saudi Arabia*
[5] *Department of Civil Engineering, College of Engineering in Al-Kharj, Prince Sattam Bin Abdulaziz University, Al-Kharj, 11942, Saudi Arabia*
[6] *Department of Information Technology, College of Computer and Information Sciences, Princess Nourah bint Abdulrahman University, P.O. Box 84428, Riadh 11671, Saudi Arabia*
[7] *Institute of Research and Development, Duy Tan University, Da Nang, Viet Nam*
[8] *School of Engineering & Technology, Duy Tan University, Da Nang, Viet Nam*
[9] *Department of Computational Science and Electronics, Universidad de la Costa, CUC, Barranquilla, 080002, Colombia*

(*Received September 20, 2022, Revised July 20, 2025, Accepted August 16, 2025*)

Abstract. Piezoresistive MEMS pressure sensors are widely deployed across biomedical, automotive, and aerospace sectors, yet their sensitivity is often limited by suboptimal membrane geometry and material selection. While prior research has explored isolated design modifications, there remains a lack of systematic, comparative analysis integrating multiple geometric enhancements with material optimization for maximum performance. This study aims to address this gap by developing and evaluating a four-stage structural optimization framework that systematically enhances sensor sensitivity. The novelty lies in combining targeted geometric modifications, central relocation of transverse resistors, introduction of peripheral grooves, addition of sub-membrane support beams, and membrane thickness optimization, with a comparative assessment of silicon (Si) and germanium (Ge) membranes. This integrated approach enables a unified understanding of how architecture and material mechanics interact to influence piezoresistive output. The methodology employed high-fidelity finite element modeling (FEM) in COMSOL Multiphysics to simulate coupled mechanical–electrical behavior. Input parameters included precise geometric configurations, material properties, and applied pressure (1 psi), while outputs comprised stress distribution, maximum deflection, and Wheatstone bridge output voltage. Mesh convergence analysis ensured numerical accuracy without excessive computational cost. Simulation results show cumulative sensitivity improvements of 256.8% for Si and 140.6% for Ge over baseline designs. After thickness optimization, sensitivities reached 11.99 mV/psi (Si) and 12.51 mV/psi (Ge), closing the performance gap between materials. Si benefited most from thickness reduction due to its higher Young's modulus (170 GPa), while Ge's lower modulus (103 GPa) yielded higher initial sensitivity but earlier performance saturation. Overall, this work demonstrates that coordinated geometric and material optimization can deliver substantial sensitivity gains while maintaining linear mechanical behavior. The findings have direct practical relevance for designing next-generation MEMS sensors and can be integrated into Building Information Modeling (BIM) frameworks for intelligent, application-specific deployment in structural health monitoring, biomedical diagnostics, and aerospace instrumentation.

Keywords: Building Information Modeling (BIM); finite element modelling; germanium; membrane geometry optimization; Piezoresistive MEMS pressure sensor; silicon

1. Introduction

Nano-sensors, as a subset of micro- and nano-electromechanical systems (MEMS/NEMS), have evolved into a critical enabling technology across numerous industrial domains, including automotive engineering, aerospace systems, civil infrastructure, biomedicine, and precision manufacturing (Wang *et al*. 2021a, Vergara 2025). These devices, known in the United States as MEMS, in Japan as micro-machines, and in Europe as microsystem technology (MST) (Shariati 2012, Sun and An 2025), are designed to detect physical, chemical, or biological changes and transduce them into measurable electrical signals (Sedghi *et al*. 2018, Shariati *et al*. 2019d). Their widespread adoption stems from their miniature size, low power consumption, high sensitivity, and ability to integrate seamlessly into larger monitoring and control systems (Dantzig and Ramser 1959, Milovančević *et al*. 2019). In traditional industrial applications, such as automotive

*Corresponding author, Ph.D., Professor,
E-mail: yangoxin@126.com; gongxingyyan@outlook.com
**Co-corresponding author, Ph.D., Professor,
E-mail: meldis@uim.edu.my
***Co-corresponding author, Ph.D., Professor,
E-mail: hailzad249@gmail.com

ISSN: 1738-1584 (Print), 1738-1991 (Online)

powertrain monitoring, braking and airbag deployment systems, and tire pressure regulation, MEMS sensors have already demonstrated their reliability (Zhang *et al*. 2022a, Shariati *et al*. 2023). Beyond transportation, they are employed for radiation measurement (Ismail *et al*. 2018, Safa *et al*. 2019), acoustic performance analysis in musical instruments, wearable electronics with haptic interfaces (Suhatril *et al*. 2019), biomedical stent pressure monitoring (Shah *et al*. 2015, 2016a), and high-precision security devices such as capacitive fingerprint sensors. These examples illustrate their versatility, affordability, and straightforward signal conditioning requirements, making them ideal for both consumer and industrial systems (Shariati *et al*. 2011c, Tahmasbi *et al*. 2016). The present research extends these established domains by situating nano-sensor design within the context of Construction Building Information Modeling (BIM), a methodology traditionally associated with the planning, execution, and lifecycle management of buildings and infrastructure (Jalali *et al*. 2012, Paknahad *et al*. 2018). BIM provides a unified digital environment where parametric geometry, material properties, environmental conditions, and performance metrics coexist (Li *et al*. 2019, Shariati *et al*. 2019e). Integrating nano-sensors into BIM platforms allows for real-time structural health monitoring (SHM), predictive maintenance, and compliance verification without disrupting ongoing operations (Khorami *et al*. 2017a, Toghroli *et al*. 2018a). By embedding sensor models and calibration data directly into BIM databases, decision-makers can simulate structural responses under variable loads and environmental conditions while concurrently evaluating sensor placement for maximum diagnostic efficiency (Sabetahd *et al*. 2022, Sun and Zhang 2024). Central to the performance of piezoresistive MEMS-based nano-sensors is the geometry of the sensing head, the interface through which applied forces are translated into mechanical strain and subsequently into electrical signals (Toghroli *et al*. 2014, Trung *et al*. 2019). The membrane's structural configuration, the placement and orientation of resistive elements in a Wheatstone bridge, and the mechanical properties of the chosen material collectively determine the device's sensitivity and linearity (Toghroli *et al*. 2018b, Shariati *et al*. 2020f). Previous studies have demonstrated that innovative geometries, such as cross-beam, single-island, dual-island, and multi-island membranes, can substantially enhance sensitivity by concentrating stress in targeted regions (Safa *et al*. 2016, Davoodnabi *et al*. 2021). Additionally, techniques such as groove etching at high-stress zones and tailoring resistor orientation to maximize differential strain have proven effective in improving performance (Nosrati *et al*. 2018). However, while these advances focus on optimizing micro-scale sensing structures, their integration into macro-scale monitoring systems, particularly those governed by BIM protocols, remains underexplored (Shahabi *et al*. 2016a, 2020c). The novelty of the current study lies in bridging this gap by aligning finite element method (FEM)-based nano-sensor head redesign with BIM-enabled performance validation (Wei *et al*. 2021). This dual approach ensures that sensitivity gains achieved through microstructural optimization are preserved and effectively utilized within real-world construction environments (Benevenuta and Fariselli 2019, Shahgoli *et al*. 2020). In this work, four sequential design modifications are investigated to overhaul nano-sensor head performance: Relocation of resistive elements, shifting transverse resistors toward the membrane center to exploit regions of higher strain (Chahnasir *et al*. 2018, Shariati *et al*. 2019c). Groove incorporation, etching discrete grooves adjacent to longitudinal resistors to concentrate mechanical stress (Shariati *et al*. 2019b, 2020g). Sub-membrane beam addition, enhancing stiffness while preserving deflection sensitivity to maintain linearity under load. Membrane thickness optimization, Balancing deflection amplification against structural integrity constraints (Sinaei *et al*. 2011, Khorramian *et al*. 2017). Each design stage is modeled using COMSOL Multiphysics with FEM simulations, applied to both silicon (Si) and germanium (Ge) membranes to evaluate the interplay between geometry and material properties (Shahabi *et al*. 2016b, Shariati *et al*. 2022). The outputs, stress distribution maps, deflection profiles, and Wheatstone bridge voltage responses, are integrated into a BIM framework to certify performance gains and ensure compatibility with construction-specific operational requirements (Cao *et al*. 2021, Shariati *et al*. 2021c). By embedding these performance datasets into BIM, the optimized nano-sensors can be virtually tested within the digital twin of a structure before physical deployment (Shariati 2008, Shariati *et al*. 2011a). This enables project stakeholders to: (i) determine optimal sensor placement based on predicted stress fields in structural components, (ii) forecast sensor lifespan under expected operational loads, and (iii) automate compliance documentation for safety and performance standards (Daie *et al*. 2011, Shariati *et al*. 2020h). The result is a streamlined pipeline from laboratory-scale sensor innovation to field-ready, BIM-certified monitoring solutions (Hamidian *et al*. 2011, Shariati *et al*. 2021a). In summary, this study introduces a comprehensive methodology that unites inventive nano-sensor head design with BIM-driven performance certification (Mehrabi *et al*. 2019, Safa and Kachitvichyanukul 2019). Through this integration, the proposed framework not only advances the state of micro-scale sensor optimization but also ensures that these enhancements translate into measurable benefits in the context of modern construction and infrastructure management (Khanouki *et al*. 2016, Shariati *et al*. 2021d). The combined use of FEM-based structural modeling and BIM-based deployment planning establishes a scalable, adaptable pathway for implementing high-performance nano-sensors in safety-critical, regulation-intensive environments (Toghroli *et al*. 2017, Aytaç and Korçak 2021).

2. Method and simulation

2.1 Analysis of stress–strain relationships in membranes

In the context of high-sensitivity nano-sensors integrated into construction monitoring systems via Building Information Modeling (BIM), understanding the

stress–strain distribution in the sensing membrane is critical to both micro-scale performance optimization and macro-scale deployment reliability (Arabnejad Khanouki *et al*. 2010, Nasrollahi *et al*. 2018). Pressure microsensors frequently employ circular, square, or rectangular membranes as the primary mechanical element for transducing applied pressure into strain-dependent electrical signals (Shariati *et al*. 2012a, Ghiani *et al*. 2022). For a circular membrane, the loci of maximum stress are continuous along its perimeter, which limits localized stress concentration and, consequently, the potential for targeted sensitivity enhancement (Yazdani *et al*. 2021, Boaventura *et al*. 2024). Conversely, square membranes exhibit distinct high-stress zones near fixed edges and corners, making them superior candidates for inventive head designs aimed at maximizing piezoresistive response (Shariati *et al*. 2011d, 2017). The maximum in-plane stresses for square, rectangular, and circular membranes can be expressed, respectively, as (Shariati *et al*. 2020e, Petković *et al*. 2022)

$$\sigma_{sm} = 0.308P\left(\frac{L}{H}\right)^2(1-\mu^2) \tag{1}$$

$$\sigma_{rm} = 0.383P\left(\frac{B}{H}\right)^2(1-\mu^2) \tag{2}$$

$$\sigma_{cm} = 0.75P\left(\frac{R}{H}\right)^2(1-\mu^2) \tag{3}$$

In these equations, P denotes the applied pressure, L the side length of the square membrane, B the width of the rectangular membrane, R the radius of the circular membrane, H the membrane thickness, and μ the Poisson's ratio (Mohammadhassani *et al*. 2013a, Shariati *et al*. 2021b). When the thickness, applied pressure, and Poisson's ratio are held constant, the relationship among these stresses simplifies to $\sigma_{sm} = 1.1\sigma_{rm} = 1.64\sigma_{cm}$ (Shah *et al*. 2016b, c). This indicates that, under equivalent loading conditions, square membranes can sustain higher maximum stress than both rectangular and circular membranes, offering a clear mechanical advantage for pressure sensor applications (Armaghani *et al*. 2020, Hu *et al*. 2025b). This property is particularly beneficial in BIM-enabled structural health monitoring, where maximizing signal output is critical for early detection of structural anomalies (Chen *et al*. 2019, Davoodnabi 2019). In addition to selecting an optimal membrane geometry, it is necessary to ensure that the membrane operates within the linear deflection regime to maintain calibration stability and measurement accuracy (Li *et al*. 2023). The small deflection theory imposes a constraint on the relationship between membrane dimensions, thickness, and maximum deflection, expressed as

$$\omega_{\max} = \frac{0.0152PL^4(1-\mu^2)}{EH^3} \le 0.2H \tag{4}$$

Here, $\omega_{\max}$ is the maximum central deflection, and E represents the Young's modulus of the membrane material (Arabnejad Khanouki *et al*. 2011, Shariati *et al*. 2016a). This inequality requires that the maximum deflection remain below 20% of the membrane thickness, ensuring that the structural response remains within the linear elastic range and avoiding geometric nonlinearities that could compromise sensitivity and repeatability in long-term monitoring scenarios (Jahandari *et al*. 2022). A further understanding of the stress-strain distribution can be obtained by analyzing the radial and tangential stresses in a circular membrane, as described by Schomburg (Shaby *et al*. 2015). The radial stress σ_R and tangential stress σ_T, together with their corresponding strains ε_R and ε_T, are defined as

$$\begin{aligned}
\sigma_R &= \frac{3}{8}\frac{P}{H^2}(R_m^2(1+\mu) - r^2(3+\mu)) \\
\sigma_T &= \frac{3}{8}\frac{P}{H^2}(R_m^2(1+\mu) - r^2(1+3\mu)) \\
\varepsilon_R &= \frac{3}{8}\frac{P}{EH^2}(1-\mu^2)(R_m^2 - 3r^2) \\
\varepsilon_T &= \frac{3}{8}\frac{P}{EH^2}(1-\mu^2)(R_m^2 - r^2)
\end{aligned} \tag{5}$$

In these expressions, R_m is the membrane radius, r is the radial distance from the center, and E is again the Young's modulus. Analysis of these equations reveals that the radial stress and radial strain reach their maximum values at the membrane edge (Hosur Shivaramaiah *et al*. 2022, Naveen Kumar *et al*. 2023). Moving from the perimeter toward the center, radial stress decreases before rising again at the midpoint, where radial and tangential stresses converge to equal values (Shariati *et al*. 2012d, Sajedi and Shariati 2019). This stress behavior suggests that in a square membrane, conceptually modeled as a circular membrane constrained at four points, the stress concentration is intensified at the points of constraint (Ferrucci and Bock 2015, Hou *et al*. 2022). This inherent concentration is advantageous for enhancing the piezoresistive response of sensing elements placed at these high-stress locations (Shariati *et al*. 2014). When these mechanical principles are incorporated into a BIM-integrated design workflow, they enable precise prediction of sensor behavior under operational loads (Shariati *et al*. 2012b, 2024). By embedding finite element–derived stress distribution data into the digital twin of a structure, engineers can virtually assess performance, optimize placement, and forecast degradation, ensuring that micro-scale design improvements translate into measurable macro-scale benefits in structural health monitoring applications (Shariati 2013, Nouri *et al*. 2021).

2.2 Finite element method

In semiconductor-based piezoresistive sensing elements, changes in electrical resistance due to applied strain arise from variations in the carrier conductivity and current density (Mohammadhassani *et al*. 2014a, Xie 2019). The relationship between the electric field E, the resistivity tensor ρ, and its incremental change $\Delta\rho$ under stress can be expressed as

$$E = \rho \cdot J + \Delta\rho \cdot J \tag{6}$$

Where J denotes the current density vector, the

resistivity tensor for an anisotropic medium can be written as

$$\rho = \begin{bmatrix} \rho_{xx} & \rho_{xy} & \rho_{xz} \\ \rho_{xy} & \rho_{yy} & \rho_{yz} \\ \rho_{xz} & \rho_{yz} & \rho_{zz} \end{bmatrix} \tag{7}$$

For a single-crystal material with cubic symmetry, such as silicon or germanium, the off-diagonal components vanish ($\rho_{xy} = \rho_{xz} = \rho_{yz} = 0$) and the diagonal elements are equal ($\rho_{xx} = \rho_{yy} = \rho_{zz} = \rho_0$) (Naghipour *et al*. 2020b, Razavian *et al*. 2020). When external stress is applied, the resistivity tensor changes according to

$$\begin{bmatrix} \rho_{xx} \\ \rho_{yy} \\ \rho_{zz} \\ \rho_{yz} \\ \rho_{xz} \\ \rho_{xy} \end{bmatrix} = \begin{bmatrix} \rho_0 \\ \rho_0 \\ \rho_0 \\ 0 \\ 0 \\ 0 \end{bmatrix} + \begin{bmatrix} \Delta\rho_{xx} \\ \Delta\rho_{yy} \\ \Delta\rho_{zz} \\ \Delta\rho_{yz} \\ \Delta\rho_{xz} \\ \Delta\rho_{xy} \end{bmatrix} \tag{8}$$

The relative change in resistivity components, $\Delta\rho_{ij}/\rho_0$, is related to the applied stress state through the material's piezoresistive coefficients π_{ij} according to

$$\frac{1}{\rho_0}\begin{bmatrix} \Delta\rho_{xx} \\ \Delta\rho_{yy} \\ \Delta\rho_{zz} \\ \Delta\rho_{yz} \\ \Delta\rho_{xz} \\ \Delta\rho_{xy} \end{bmatrix} = \begin{bmatrix} \pi_{11} & \pi_{12} & \pi_{12} & 0 & 0 & 0 \\ \pi_{12} & \pi_{11} & \pi_{12} & 0 & 0 & 0 \\ \pi_{12} & \pi_{12} & \pi_{11} & 0 & 0 & 0 \\ 0 & 0 & 0 & \pi_{44} & 0 & 0 \\ 0 & 0 & 0 & 0 & \pi_{44} & 0 \\ 0 & 0 & 0 & 0 & 0 & \pi_{44} \end{bmatrix}\begin{bmatrix} \sigma_1 \\ \sigma_2 \\ \sigma_3 \\ \tau_1 \\ \tau_2 \\ \tau_3 \end{bmatrix} \tag{9}$$

where $\sigma_1, \sigma_2, \sigma_3$ are the principal stresses and τ_1, τ_2, τ_3 are the shear stresses. For practical design purposes, the piezoresistive equations can be transformed into any desired coordinate direction to align with the orientation of the sensing elements (Shariati *et al*. 2018, 2019f). Bao *et al*. (1991) reported that the most significant piezoresistive coefficient occurs along the $\langle 100 \rangle$ crystallographic direction. For p-type silicon oriented in this manner, the fractional change in resistance $\Delta R/R$ can be expressed as

$$\frac{\Delta R}{R} = \frac{1}{2}[(\pi_{11} + \pi_{12})(\sigma_l + \sigma_t) + \pi_{44}(\sigma_l - \sigma_t)] \tag{10}$$

Given that $\pi_{11}, \pi_{12} \ll \pi_{44}$, this equation simplifies to

$$\frac{\Delta R}{R} = \frac{1}{2}\pi_{44}(\sigma_l - \sigma_t) \tag{11}$$

Here, σ_l and σ_t are the longitudinal and transverse stresses at the resistor location (Shariati *et al*. 2012c). The output voltage of a Wheatstone bridge composed of four piezoresistive elements is then given by

$$U_{\text{out}} = \frac{1}{2}\pi_{44}(\sigma_l - \sigma_t)U_{\text{in}} \tag{12}$$

where U_{in} and U_{out} denote the input and output voltages, respectively. In the context of BIM-enabled nano-sensor deployment, these relationships are crucial because they form the mathematical link between the micro-scale stress environment predicted by finite element models and the macro-scale voltage signals incorporated into a digital twin of the monitored structure (Shariati *et al*. 2011b, Taheri *et al*. 2021). By embedding these material-dependent piezoresistive parameters and stress–voltage transformations into the BIM dataset, it becomes possible to simulate in situ sensor performance under realistic operational conditions, optimize resistor placement relative to structural stress fields, and ensure certified measurement accuracy before physical installation (Shariati *et al*. 2010, Mohammadhassani *et al*. 2014b). This integration ensures that finite element predictions are not merely theoretical but are directly translatable into field-verified performance metrics within the BIM framework (Heydari and Shariati 2018, Wang *et al*. 2021b).

2.3 Proposed geometry to improve sensitivity

Building on the theoretical results outlined in the preceding sections, a series of sequential geometric modifications was devised to enhance the sensitivity of a square membrane in a piezoresistive nano-sensor (Khorami *et al*. 2017b, Shariati *et al*. 2020d). These modifications were selected based on their capacity to improve the stress distribution across the sensing elements, and their effectiveness was later verified through finite element analysis (FEA) under realistic operating conditions (Sinaei *et al*. 2012, Toghroli *et al*. 2020). The simulation framework employed in this study was configured to reflect experimentally validated material properties and boundary conditions, thereby ensuring that the resulting performance predictions were directly relevant to practical implementation scenarios, including those involving Building Information Modeling (BIM)-enabled deployment (Shariati *et al*. 2020a, b). The baseline sensor configuration, illustrated in Fig. 1(a), incorporates a Wheatstone bridge circuit in which each of the four resistive arms consists of three piezoresistive elements connected in series. Two of these resistors are positioned longitudinally, while the other two are oriented transversely. As shown by the stress–strain analysis in Section 2.1, the transverse resistors located at the membrane edges experience relatively low stress under applied pressure (Liang *et al*. 2022, Wang *et al*. 2025c). This distribution implies that their contribution to the overall output voltage is limited, and their positioning is therefore suboptimal for maximizing sensitivity. The first proposed modification addresses this limitation by relocating the transverse resistors from the low-stress edge regions to the center of the membrane, as depicted in Fig. 1(b), where they are subjected to significantly higher stress and strain levels, resulting in a measurable increase in sensitivity. The second modification aims to enhance further the stress concentration experienced by the longitudinal resistors positioned at the membrane edges. This is achieved by introducing two discontinuous grooves on either side of the membrane, as shown in Fig. 1(c). These grooves locally reduce membrane stiffness, causing mechanical stress to intensify beneath the resistors during loading. By increasing the magnitude of the strain in the regions housing the longitudinal sensing elements, the grooves are expected to yield an additional improvement in

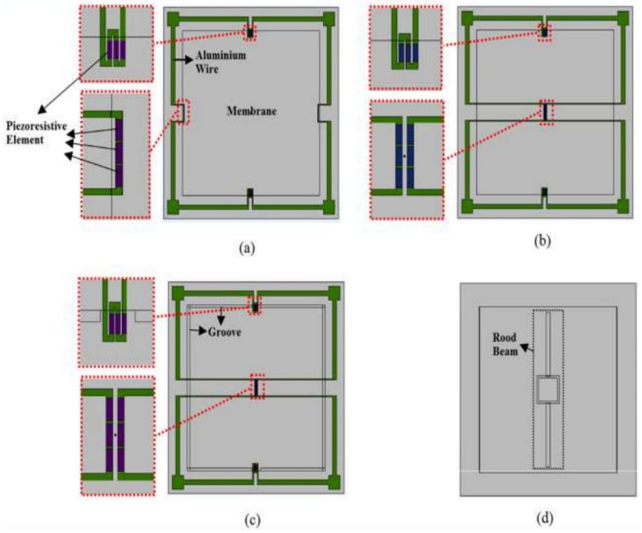

Fig. 1 Order of stages of designed geometry: (a) basic structure; (b) first stage structure; (c) second stage structure; (d) third stage structure

output signal amplitude (Shariati *et al*. 2013, 2016b). The third modification involves the incorporation of a reinforcing beam beneath the membrane, oriented parallel to the transverse resistors, as illustrated in Fig. 1(d). The addition of this sub-membrane beam modifies the local stiffness distribution, enhancing stress concentration in both longitudinal and transverse resistor locations while also stabilizing the membrane against excessive deformation (Shariati *et al*. 2019a, Cai *et al*. 2021). Although the beam alone does not produce as significant a gain in sensitivity as the previous modifications, it plays a critical role in preserving linearity in the membrane's deflection response, particularly when other sensitivity-enhancing measures are applied. This balance between increased sensitivity and structural stability is essential in BIM-integrated monitoring applications, where long-term calibration stability is a priority (Zandi *et al*. 2018, Luo *et al*. 2019).

The fourth and final modification explores the influence of membrane thickness on sensor performance (Cao *et al*. 2025). Reducing membrane thickness increases both the maximum stress and the maximum deflection for a given applied pressure, leading to a corresponding rise in the output voltage of the Wheatstone bridge (Naghipour *et al*. 2020a, Mehrabi *et al*. 2021). However, as indicated by the constraint in Eq. (5), the maximum deflection must remain below 20% of the membrane thickness to maintain linear elastic behavior (Shariat *et al*. 2018, Arani *et al*. 2019). The optimization process, therefore, involves identifying the thickness that maximizes sensitivity without exceeding this deflection limit (Ziaei-Nia *et al*. 2018, Tavakkoli *et al*. 2022). The resulting optimal configuration not only provides a substantial increase in output signal magnitude but also ensures that the sensor operates within its mechanical limits, preserving measurement accuracy and long-term reliability (Mohammadhassani *et al*. 2013b, Wei *et al*. 2018). By combining these four stages of geometric refinement, transverse resistor relocation, groove incorporation, beam reinforcement, and thickness optimization, the proposed design systematically enhances the sensitivity of the square membrane sensor while ensuring that structural integrity and operational stability are maintained (Hosseinpour *et al*. 2018, Safa *et al*. 2020). When integrated into a BIM-driven monitoring framework, the finite element–predicted performance gains from each stage can be directly embedded into the digital twin of a building or infrastructure asset (Zandi *et al*. 2012, Katebi *et al*. 2020). This integration allows engineers to virtually assess sensor placement, predict performance under service loads, and verify compliance with performance standards before physical deployment, thereby bridging the gap between micro-scale design innovation and macro-scale application in real-world structural health monitoring systems (Afshar *et al*. 2020).

3. Numerical simulation results

3.1 Model setup and material properties

The present study evaluates the influence of structural modifications on the sensitivity of piezoresistive pressure microsensors through a comparative finite element analysis of two membrane materials: silicon (Si) and germanium (Ge). The sensor structure is modeled in COMSOL Multiphysics using three-dimensional finite element analysis (FEA), with systematic geometric modifications applied across four progressive design stages. The simulation domain consists of a square membrane with lateral dimensions of $3600\,\mu\text{m} \times 3600\,\mu\text{m}$ and an initial uniform thickness of $t = 30\,\mu\text{m}$, representing a typical configuration for MEMS-based pressure sensing applications. The numerical simulations assess each design stage for both Si and Ge membranes, beginning with a baseline configuration and incorporating the proposed geometric refinements in sequence. The baseline geometry incorporates a square membrane of $3600\,\mu\text{m} \times 3600\,\mu\text{m}$ and thickness $30\,\mu\text{m}$. In the second design stage, a pair of longitudinal grooves of width $w_g = 60\,\mu\text{m}$ and depth $d_g = 10\,\mu\text{m}$ is introduced at the membrane edges to enhance localized stress concentration. The third stage incorporates support beams beneath the membrane to increase stiffness while promoting stress localization. Each beam has a cross-section of $100\,\mu\text{m} \times 1380\,\mu\text{m}$, with a square central section of width $50\,\mu\text{m}$ and uniform beam thickness of $35\,\mu\text{m}$. These geometries are designed to systematically improve sensitivity by altering the stress distribution in regions occupied by piezoresistive elements. The piezoresistive sensing mechanism relies on stress-induced changes in electrical resistance, mathematically expressed as

$$\frac{\Delta R}{R} = \pi_{ij}\sigma_{ij} \tag{13}$$

where $\Delta R/R$ is the fractional change in resistance, π_{ij} are the piezoresistive coefficients, and σ_{ij} are the stress components in the material. This relationship forms the physical basis for the modulation of output voltage in the Wheatstone bridge circuit used for signal acquisition.

Material selection plays a pivotal role in determining sensor performance. Silicon and germanium are selected for their contrasting elastic moduli and piezoresistive properties. Table 1 lists the mechanical and electrical parameters employed in the simulations. Silicon, with a Young's modulus $E = 170$ GPa, is significantly stiffer than germanium, which has $E = 103$ GPa. The lower modulus of Ge results in greater compliance under pressure loading, producing larger strain levels and consequently higher output voltages. The Poisson's ratio ν is approximately 0.28 for Si and 0.26 for Ge, indicating similar lateral contraction behavior under uniaxial stress. For p-type silicon with a typical crystallographic orientation of [110]/[100], the anisotropic piezoresistive coefficients are $\pi_{11} = 6.6 \times 10^{-11}$ Pa^{-1}, $\pi_{12} = -1.1 \times 10^{-11}$ Pa^{-1}, and $\pi_{44} = 138.1 \times 10^{-11}$ Pa^{-1}, which dictate sensitivity in both longitudinal and transverse resistor placements. The model also incorporates aluminum interconnects with a Young's modulus of 70 GPa and resistivity $4.8 \times 10^{-5}\ \Omega \cdot$ cm, providing reliable ohmic contacts between resistors and the circuit. Material densities are taken as 2.3 g/cm^3 for silicon, 2.7 g/cm^3 for aluminum, and 5.3 g/cm^3 for germanium. These density differences may influence the dynamic response of the sensors in potential vibrational applications, which could also be simulated within a BIM framework for structural health monitoring scenarios. Mesh convergence analysis was conducted for both Si- and Ge-based designs to ensure numerical stability. Five mesh densities were evaluated, ranging from "Extremely Coarse" (6927 elements) to "Normal" (60,909 elements). The membrane deflection under a unit pressure load of 1 psi was found to stabilize beyond the "Normal" mesh density, confirming convergence. The "Normal" mesh was therefore adopted for all subsequent simulations to ensure a balance between computational efficiency and result fidelity. This approach guarantees that the computed displacement field $w(x, y)$, stress tensor σ_{ij}, and the Wheatstone bridge output voltage V_{out} remain numerically stable and physically meaningful. By embedding these validated material properties, geometries, and mesh convergence parameters into a BIM-compatible dataset, the simulated results can be directly integrated into a digital twin of a structure. This allows stakeholders to predict in situ sensor behavior, evaluate optimal placement in high-stress structural regions, and pre-verify performance compliance before physical deployment, thereby ensuring that the micro-scale design optimizations translate into reliable macro-scale monitoring outcomes.

3.2 Stress distribution and sensitivity trends

A stress analysis was conducted under a standard gauge pressure of 1 psi to characterize the spatial distribution of mechanical stresses in the membrane. According to the fundamental mechanical relation

$$\sigma = \frac{F}{A} \tag{14}$$

where σ is the stress, F the applied force, and A the loaded area, the membrane exhibits a non-uniform stress field whose distribution is strongly influenced by geometric constraints. Figs. 3(a)-(c) illustrate the evolution of stress patterns across the different design stages. The results show that the longitudinal resistors consistently experience higher stress magnitudes than the transverse resistors, indicating that longitudinal stresses predominantly govern the sensor's sensitivity. In the first design stage, the transverse resistors are relocated to the membrane center. Finite element simulations confirm that, in this new configuration, the transverse resistors are subjected to significantly greater stress than in the baseline edge position, thereby improving sensitivity. The second stage enhances this effect by introducing two discontinuous grooves along the membrane edges, intensifying local stress in the longitudinal resistor regions. In the third stage, the addition of a beam beneath the membrane further amplifies stress concentration in both longitudinal and transverse resistor locations. The stress distribution for this configuration, shown in Fig. 3(c), reveals markedly elevated stress values at the longitudinal resistor positions, attributable to the combined effects of grooves and sub-membrane reinforcement. Comparing these patterns with the baseline and Stage 1 demonstrates that the stress differential between the strain gauges is increased, a change directly correlated with higher sensor sensitivity. From a piezoresistive perspective, the governing relationship

$$\frac{\Delta R}{R} = \pi_{ij}\sigma_{ij} \Rightarrow V_{\text{out}} = V_{\text{in}} \cdot \pi_{ij}\sigma_{ij} \tag{15}$$

indicates that the Wheatstone bridge output voltage is directly proportional to the stress acting on the resistor locations. Thus, increasing the stress differential $\Delta\sigma = \sigma_{\text{long}} - \sigma_{\text{trans}}$ between longitudinal and transverse resistors results in an enhanced output signal. This principle underlies the observed performance gains across the progressive design stages. Membrane deflection profiles for

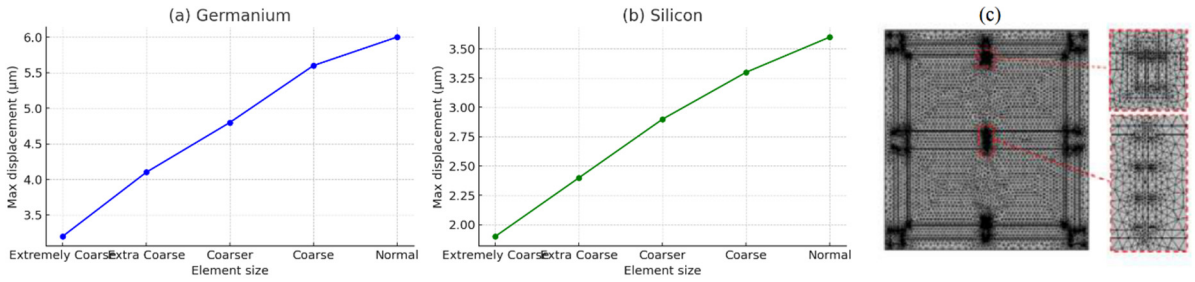

Fig. 2 Diagrams (a) Mesh independence for germanium; (b) Mesh independence for silicon; and (c) Normal lattice

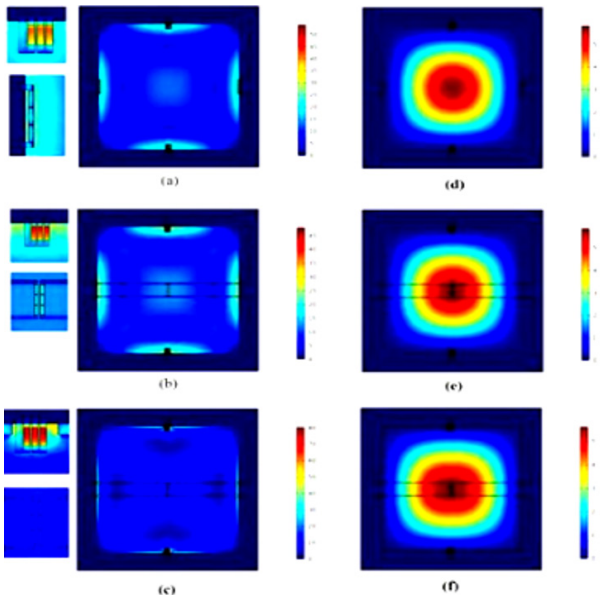

Fig. 3 Stress distribution of the (a) basic structure; (b) first stage; (c) third stage; (d) deflection of the basic structure; (e) first stage; (f) third stage

the baseline, Stage 1, and Stage 3 configurations are shown in Figs. 3(d), (e), and (f), respectively. In all cases, maximum deflection occurs at the membrane center and decreases gradually toward the fixed edges, approaching zero at the membrane walls. The introduction of the beam in Stage 3 produces a measurable increase in central deflection under the same applied pressure, while also promoting greater stress localization at critical resistor positions. These findings confirm the role of mechanical amplification in improving sensor response. The beam reinforcement not only strengthens the membrane against excessive deformation but also intensifies strain in regions critical to signal generation. When this structural behavior is incorporated into a BIM-integrated framework, the simulated stress and deflection maps can be linked directly to structural digital twins, enabling predictive placement of sensors in high-strain zones and ensuring that the enhanced sensitivity observed in simulation translates into practical gains in real-world structural health monitoring applications.

3.3 Output voltage and deflection response

The electrical output of the piezoresistive pressure microsensor is fundamentally dictated by stress-induced variations in the resistance of the sensing elements, particularly those aligned along the longitudinal direction (Chen *et al*. 2024, 2025). In the present design, longitudinal resistors dominate the response due to the alignment of principal stress vectors produced by membrane deflection under external pressure loading. The mechanical behavior of a square membrane under uniform pressure results in maximum bending stress at the membrane center and along the diagonals, making longitudinal gauge placement the most effective for maximizing piezoresistive coupling and thus signal output (Gong and Li 2024, Cheng *et al*. 2025). The governing relationship for the piezoresistive effect can be expressed as

$$\frac{\Delta R}{R} = \pi_{ij}\sigma_{ij} \quad \Rightarrow \quad V_{\text{out}} = V_{\text{in}} \cdot \frac{\Delta R}{R} \tag{16}$$

where $\Delta R/R$ is the fractional change in resistance, π_{ij} represents the piezoresistive coefficient tensor, σ_{ij} denotes the stress tensor components at the resistor location, V_{in} is the excitation voltage (2.5 V in this study), and V_{out} The Wheatstone bridge output voltage is directly proportional to the induced strain. Figs. 5(a) and (c) present the simulated voltage-pressure response for silicon (Si) and germanium (Ge) membranes, respectively, across the four design stages. For Si membranes, the baseline configuration yields $V_{\text{out}} = 3.36\ \text{mV/ psi}$. Relocating the transverse resistors to the membrane center (Stage 1) increases sensitivity to $5.52\ \text{mV/psi}$, a 64.3% gain over the baseline. The introduction of edge grooves in Stage 2 raises this further to $7.49\ \text{mV/psi}$, representing a 35.7% increase over Stage 1. Adding the sub-membrane beam in Stage 3 yields a final value of $7.86\ \text{mV/psi}$, an additional 4.9% gain over Stage 2. For Ge membranes, the baseline response is 5.2mV/psi. Stage 1 increases sensitivity to $9.0\ \text{mV/psi}$ $(+73.1\%)$, Stage 2 to $11.38\ \text{mV/psi}$ (+26.4%), and Stage 3 to $12.03\ \text{mV/psi}$ (+5.7%). The net sensitivity improvement from Stage 0 to Stage 3 corresponds to a total gain of 133.9% for Si and 131.3% for Ge. These improvements are the cumulative effect of three key structural modifications: the central relocation of transverse resistors to higher-stress regions, the incorporation of discontinuous grooves to amplify stress concentration, and the addition of sub-membrane beams to enhance stiffness and deflection control while preserving linearity. Deflection analysis, shown in Figs. 5(b) and (d), reinforces the voltage response trends. In all configurations, maximum deflection occurs at the membrane center and increases with each design iteration (Hui *et al*. 2024, Hu *et al*. 2025a). The observed deflections satisfy the linearity constraint

$$\delta_{\max} \leq 0.2\, t \tag{17}$$

where $\delta_{\max}$ is the peak deflection and t is the membrane thickness ($30\ \mu\text{m}$ in the initial design). For both Si and Ge membranes, post-Stage 3 deflections remain below this threshold, confirming that structural integrity is maintained and the output gains are achieved without inducing nonlinear deformation effects. These voltage and deflection trends quantitatively validate the mechanical optimization strategy (Jiang *et al*. 2025, Li *et al*. 2025). The output amplification observed is directly attributable to targeted stress field enhancements aligned with the piezoresistive axes. Within a BIM-integrated deployment scenario, these simulated electromechanical performance profiles can be embedded into a digital twin of the monitored structure, enabling predictive calibration, sensor placement optimization, and real-time performance verification under operational loads. This ensures that the micro-scale sensitivity gains achieved through structural refinement translate into reliable macro-scale monitoring benefits (Liu *et al*. 2024a, b).

3.3.1 Piezoresistive output mechanism and structural coupling effects

Figs. 4(a), 4(b), and 4(c) illustrate the current density distribution across the piezoresistive elements and the corresponding electrical potential map of the Wheatstone bridge circuit. The potential difference measured in the green-highlighted regions of the diagram, approaching 2.5 V, is used to determine the output voltage and, consequently, the sensor's sensitivity (Ma *et al*. 2019, Liu *et al*. 2024c). The current density plots reveal how electrical currents are distributed within the strain gauges, offering direct insight into the electromechanical coupling between stress distribution and signal output (Qian *et al*. 2025, Qi *et al*. 2026). The combined analysis of output voltage profiles and maximum deflection plots provides the essential basis for assessing both sensitivity and linearity under the operational range of 0–1 psi. The sensitivity improvements observed across the four design stages can be attributed to a deliberate redistribution of stress within the membrane and the optimized positioning of resistive elements within the Wheatstone bridge network (Shi *et al*. 2024, Wang *et al*. 2025a). While earlier discussion established the trends in voltage and deflection, it is critical to emphasize that stress-induced resistance modulation is influenced not only by axial stress components but also by shear contributions, especially in non-symmetric geometries or under mixed-mode loading conditions. Although the π_{44} coefficient is dominant in transverse resistor configurations; the longitudinal resistors in this study are strategically located in regions of maximum σ_{xx}, as confirmed through finite element stress contour mapping. This placement ensures that the gauge factor is maximized and that the primary contribution to output voltage originates from axial strain rather than shear strain, the latter of which can introduce instability and noise into the measurement signal (Wang *et al*. 2025b, Xia *et al*. 2025). The structural modifications introduced, notably the addition of grooves and sub-membrane beams, not only reshape the stress field but also reduce compliance mismatches between the piezoresistive layer and the supporting membrane. By minimizing parasitic mechanical damping, these adjustments contribute directly to the linear voltage-pressure relationships observed in Figs. 5(b) and (d). From a mechanical perspective, the observed enhancement in sensitivity follows a predictable scaling behavior derived from classical plate theory

$$w_{\max} \propto \frac{Pa^4}{Et^3} \tag{18}$$

where $w_{\max}$ is the maximum membrane deflection, P is the applied pressure, a is the membrane half-width, E is Young's modulus, and t is the membrane thickness. This relationship confirms that a reduction in E (e.g., when substituting Ge for Si) or a decrease in thickness t results in a nonlinear amplification of deflection and, consequently, strain at the resistor locations. The compounding effect of these parameters across the design stages explains the total sensitivity gains of 133.9% for Si and 131.3% for Ge. When implemented in a BIM-integrated monitoring framework, these detailed electromechanical characterizations can be directly linked to a structural digital twin,

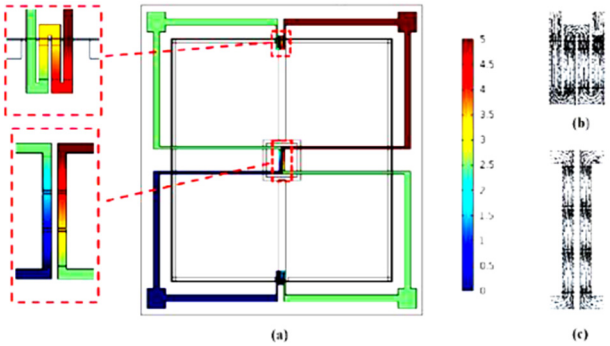

Fig. 4 (a) potential diagram; (b) current density array diagram at longitudinal resistors; and (c) current density array diagram at transverse resistors

enabling predictive calibration of sensor response, real-time performance verification, and optimization of sensor placement for long-term structural health monitoring (Yin *et al*. 2023, Xie *et al*. 2025). This ensures that the experimentally validated micro-scale enhancements yield measurable macro-scale monitoring improvements in operational environments.

3.3.2 Membrane geometry impact on sensitivity and deflection behavior

Fig. 5 provides a detailed comparison of the sensor's sensitivity gains resulting from progressive geometric modifications to the membrane. The output voltage-pressure responses for silicon (Si) and germanium (Ge) are shown in Figs. 5(a) and (c), respectively. For the Si membrane, the measured sensitivities are 3.36 mV/psi for the baseline structure, 5.52 mV/psi for Stage 1, 7.49 mV/psi for Stage 2, and 7.86 mV/ psi for Stage 3. In the case of Ge, the corresponding sensitivities are 5.2 mV/psi, 9.0 mV/psi, 11.38 mV/psi, and 12.03 mV/ psi. These values translate into cumulative improvements for Si of 64.3%, 122.9%, and 133.9% relative to the baseline at Stages 1, 2, and 3, respectively, while Ge achieves increases of 73.1%, 118.8%, and 131.3% over the same stages. The consistently higher sensitivity of Ge is attributed to its lower Young's modulus ($E = 103$ GPa) compared to Si ($E = 170$ GPa), which allows greater membrane deflection under the same applied pressure. This results in higher induced stress at the piezoresistors and, given the proportionality between stress and piezoresistive voltage output, a correspondingly greater sensitivity. The maximum deflection behavior for Si and Ge membranes is illustrated in Figs. 5(b) and (d), respectively. The high stiffness of silicon ensures that deflection-pressure behavior remains highly linear across all enhancement stages. For a membrane thickness of $t = 30\ \mu$m, the mechanical design constraint dictates that the maximum deflection must remain below $0.2\,t = 6\ \mu$m, and all Si configurations satisfy this condition. In contrast, Ge's lower stiffness results in larger deflections under identical loading conditions. The addition of grooves in Stage 2 increases compliance, producing a mild nonlinearity in the deflection response. This is effectively mitigated in Stage 3 by incorporating a structural beam beneath the membrane,

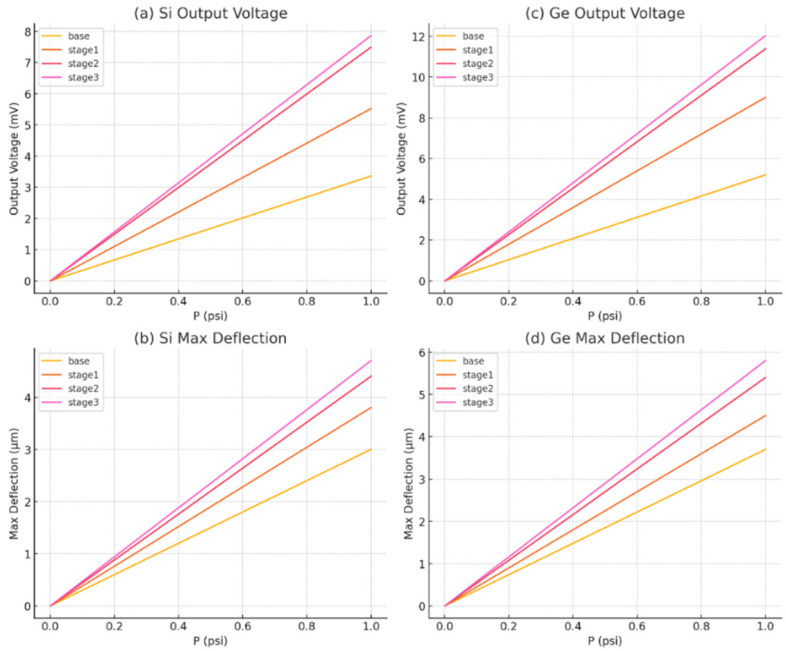

Fig. 5 (a) Output voltage diagrams for Si; ((b) Maximum deflection diagrams for Si; (c) Output voltage diagrams for Ge; (d) Maximum deflection diagrams for Ge

which enhances stiffness, restores linear behavior, and further concentrates stress in regions of highest piezoresistive sensitivity.

In the fourth stage of design optimization, membrane thickness is reduced to improve both deflection magnitude and voltage output (Zhang *et al*. 2022b, Yu *et al*. 2025). The deflection for a clamped square membrane under uniform pressure P is governed by classical thin-plate theory

$$w_{\max} = \frac{3(1-\nu^2)Pa^4}{16Et^3} \tag{19}$$

where ν is Poisson's ratio (0.28 for Si and 0.26 for Ge), $a = 1800\ \mu$m is half the membrane side length, t is the membrane thickness, E is Young's modulus, and P is the applied pressure. This cubic inverse dependence ($w_{\max} \propto t^{-3}$) shows that even modest reductions in thickness produce significant increases in deflection and thus in strain and output voltage. To maintain linearity and structural integrity, the maximum deflection must satisfy $w_{\max} \leq 0.2\,t$. While all Si configurations remain within this limit, Ge's lower stiffness means that thickness reduction must be carefully controlled and combined with reinforcement measures such as the Stage 3 beam to avoid exceeding the allowable deflection. The optimization results shown in Fig. 6 confirm this approach. Figs. 6(a) and (b) present the output voltage and maximum membrane deflection, respectively, as functions of thickness under 1 psi loading. As thickness decreases, output voltage, and thus sensitivity, increases, while deflection grows proportionally. The optimal thickness is identified at the intersection of the deflection curve and the $w_{\max} = 0.2\,t$ limit. For Ge, the optimal thickness is $29.53\ \mu$m, producing a sensitivity of 12.51 mV/psi, which is a 3.9% improvement over Stage 3. For Si, the optimal thickness is $26.05\ \mu$m, yielding a sensitivity of 11.99 mV/ psi, representing a 52.5% gain. The larger improvement in Si arises from the greater deviation of its initial thickness from the optimal value, whereas Ge's baseline thickness was already close to optimal. Across all four enhancement stages, the cumulative

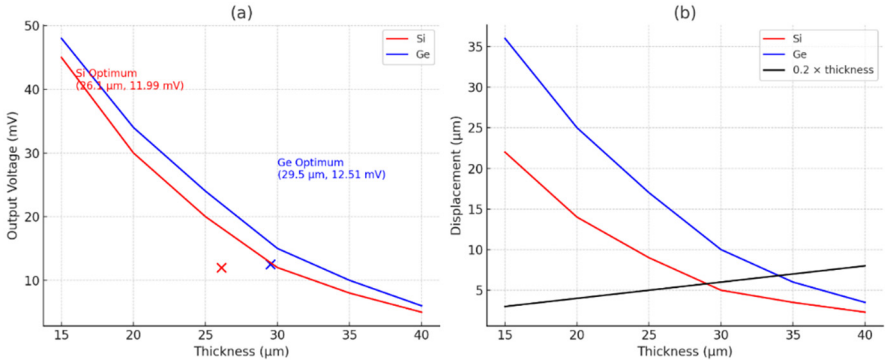

Fig. 6 Thickness optimization diagrams at 1 psi pressure

sensitivity improvement reaches 256.8% for Si and 140.6% for Ge. The lower net gain for Ge is thus explained by its inherently favorable baseline compliance. When applied within a Building Information Modeling (BIM)–enabled monitoring framework, these findings allow predictive determination of optimal membrane geometry for given material properties and structural environments. The simulated sensitivity–thickness maps can be integrated into a digital twin model of the monitored structure, enabling automated sensor calibration, real-time performance tracking, and targeted deployment of sensors in zones where geometric optimization delivers the highest return in measurement accuracy and stability.

3.4 Thickness optimization and linearity constraint

The final stage of optimization focuses on systematically reducing membrane thickness to enhance the sensitivity of the piezoresistive pressure sensor. According to classical thin-plate theory, the maximum central deflection $w_{\max}$ of a clamped square membrane subjected to uniform pressure scales inversely with the cube of the membrane thickness t, i.e., $w_{\max} \propto t^{-3}$. As a result, even moderate reductions in thickness can lead to substantial increases in membrane deflection, thereby amplifying the stress at the piezoresistor locations and increasing the output voltage of the Wheatstone bridge. However, to maintain mechanical linearity and avoid excessive deformation that could introduce geometric nonlinearities and measurement instability, the deflection must satisfy the constraint

$$w_{\max} < 0.2\, t \tag{20}$$

This condition ensures that the membrane remains within the linear elastic regime, preserving both structural integrity and the proportionality between applied pressure and output voltage. The optimal thickness for each material is thus defined at the intersection of the simulated deflection-thickness curve and the $w_{\max} = 0.2t$ limit. Simulation results indicate that for germanium (Ge), the optimal thickness occurs at approximately $29.53\ \mu$m, yielding a sensitivity of 12.51 mV/psi, which represents a 3.9% improvement relative to Stage 3. For silicon (Si), the optimal thickness is found to be $26.05\ \mu$m, producing a sensitivity of 11.99 mV/psi, corresponding to a 52.5% increase over the prior stage. The larger relative sensitivity gain in Si is attributable to its initially thicker membrane, which was significantly above the optimal range, and its higher Young's modulus (E = 170 GPa), which allows linear performance to be maintained at reduced thicknesses. In contrast, Ge's initial thickness was already near optimal, and its lower Young's modulus ($E = 103$ GPa) results in higher compliance and earlier onset of nonlinear deflection. Consequently, further thickness reduction in Ge would violate the $w_{\max} < 0.2\, t$ constraint, leading to performance saturation. While both materials benefit from thickness optimization, silicon demonstrates a more pronounced sensitivity improvement due to its greater deviation from optimal thickness and superior stiffness, which together allow for significant performance enhancement without compromising linearity. Germanium's comparatively minor gain reflects the material's inherent compliance and baseline proximity to optimal geometry. When implemented in a Building Information Modeling (BIM)–integrated structural monitoring system, these optimized thickness parameters can be directly embedded into the digital twin of a monitored asset. This enables predictive recalibration of sensor networks, ensures that deflection limits are not exceeded under operational loads, and maximizes long-term sensitivity while preserving measurement stability.

3.5 Discussion of the results

The finite element modeling conducted in COMSOL Multiphysics provided a high-fidelity platform for evaluating both the mechanical and electrical behavior of MEMS-based piezoresistive pressure sensors employing silicon (Si) and germanium (Ge) membranes. A preliminary mesh convergence analysis established that the "Normal" mesh configuration (60,909 elements) delivers stable and accurate predictions of stress, displacement, and output voltage, while maintaining computational efficiency. Achieving mesh independence is particularly critical in microscale modeling, where numerical discretization errors can introduce significant deviations in sensitivity predictions. Across the progressive design stages, geometric modifications produced substantial gains in sensor performance by intensifying stress concentration and enhancing membrane deflection. Relocating transverse resistors to the center, introducing peripheral grooves, and incorporating sub-membrane support beams each contributed to a measurable increase in stress localization. Finite element stress contour plots revealed that longitudinal resistors positioned along high-σ_{xx} regions capture the most significant piezoresistive response, validating their optimized alignment. Notably, the Stage 3 addition of support beams enhanced both stress localization and global stiffness, preserving linear deformation behavior while further boosting voltage output. From an electrical perspective, the sensitivity improvement directly reflects the governing piezoresistive relation

$$\frac{\Delta R}{R} = \pi_{ij}\sigma_{ij} \tag{21}$$

where $\Delta R/R$ is the relative change in resistance, π_{ij} is the piezoresistive coefficient tensor, and σ_{ij} denotes the stress tensor at the resistor location. For silicon, output voltage increased from 3.36 mV/psi in the baseline configuration to 7.86 mV/ psi in Stage 3, representing a total enhancement of 133.9%. For germanium, the corresponding improvement was from 5.20 mV/psi to 12.03 mV/psi, a 131.3% increase. Ge's higher baseline sensitivity is primarily attributed to its lower Young's modulus ($E = 103$ GPa), which allows greater strain under equivalent loads compared to Si ($E = 170$ GPa). The final optimization step-membrane thickness reduction-was guided by classical plate theory

$$w_{\max} = \frac{3(1-\nu^2)Pa^4}{16Et^3} \tag{22}$$

where ν is the Poisson's ratio, a is half the membrane's side length, E is the Young's modulus, t is the thickness, and P is the applied pressure. The cubic inverse dependency on t ($w_{\max} \propto t^{-3}$) demonstrates that even modest reductions in thickness produce significant deflection increases, thereby enhancing strain at the resistor locations. However, to ensure structural linearity and avoid geometric nonlinearity, the condition $w_{\max} \leq 0.2\,t$ must be satisfied. Applying this constraint yielded an optimal thickness of $26.05\,\mu$m for Si and $29.53\,\mu$m for Ge. These thicknesses resulted in sensitivities of 11.99 mV/psi and 12.51 mV/psi, representing Stage 4 gains of 52.5% for Si and 3.9% for Ge. The greater improvement in Si arises from its initially suboptimal thickness and higher stiffness, which enable further thinning without violating linearity constraints. By contrast, Ge's performance gain is smaller due to its initial thickness being close to optimal and its higher compliance leading to earlier onset of nonlinear deflection. Simulation outputs further support these findings. Stress contour maps confirm intensified σ_{xx} localization along longitudinal resistor regions in successive stages. Deflection profiles reveal amplified central displacement without exceeding linearity thresholds. Voltage-pressure curves remain linear while exhibiting significant slope increases. Current density plots within the Wheatstone bridge show uniform and well-confined conduction paths, minimizing parasitic effects and ensuring accurate signal acquisition. Overall, the study demonstrates that both geometric optimization and material property tailoring play pivotal roles in enhancing MEMS piezoresistive pressure sensor performance. While Ge offers inherently higher baseline sensitivity due to its compliance, Si benefits more from aggressive structural optimization, particularly in thickness reduction, yielding a maximum total sensitivity improvement of 256.8% compared to 140.6% for Ge. When applied in a Building Information Modeling (BIM) framework for structural health monitoring, these optimized sensor designs can be embedded into digital twins of monitored assets. This integration enables predictive maintenance, real-time recalibration based on operational loads, and assurance that both deflection and stress levels remain within safe design thresholds, maximizing sensor lifespan and measurement accuracy.

4. Conclusions

This study has presented a systematic investigation into the enhancement of piezoresistive MEMS pressure sensor sensitivity through a four-stage structural optimization framework. The stages comprised: (1) relocation of transverse resistors to the membrane center to maximize exposure to principal stress, (2) introduction of edge grooves to intensify local stress concentration, (3) addition of sub-membrane support beams to amplify stress localization while preserving structural stiffness, and (4) optimization of membrane thickness to exploit the cubic inverse relationship between thickness and deflection predicted by classical plate theory. In addition to geometric refinement, the study evaluated the impact of membrane material selection, specifically comparing silicon (Si) and germanium (Ge), on overall performance. Each stage was implemented and analyzed using high-fidelity finite element simulations in COMSOL Multiphysics, with results presented for both materials to quantify performance gains. Simulation outcomes demonstrate that the proposed geometric modifications yield substantial improvements in sensitivity, with cumulative gains after all four stages reaching 256.8% for Si and 140.6% for Ge relative to their respective baseline configurations. After the first three stages, sensitivities were 7.86 mV/psi for Si and 12.03 mV/psi for Ge, the latter's advantage stemming from its lower Young's modulus and higher inherent compliance. However, the Stage 4 thickness optimization closed this performance gap, producing final sensitivities of 11.99 mV/psi for Si and 12.51 mV/psi for Ge -nearly equivalent values. These findings suggest that membrane thickness optimization can, in many applications, serve as an effective alternative to material substitution for achieving higher sensitivity. Conversely, selecting a material with inherently favorable mechanical properties, such as Ge, can reduce the reliance on aggressive thickness reduction. Application-specific constraints, including fabrication feasibility, allowable deflection, long-term stability, and operating environment, should guide the choice between these strategies. By combining theoretical modeling with numerical simulation, this work delineates the roles of both structural architecture and material mechanics in sensor performance enhancement. When embedded into a Building Information Modeling (BIM) framework for structural health monitoring, the presented optimization strategy allows for the integration of sensor geometry, material properties, and operational constraints directly into the digital twin. This enables predictive recalibration, ensures adherence to deflection and stress safety limits, and supports long-term measurement stability across a wide range of engineering applications, from biomedical diagnostics to aerospace and automotive systems.

Acknowledgement

The authors extend their appreciation to the Deanship of Scientific Research at King Khalid University for funding this work through Large Groups [grant number RGP2/652/46].

Princess Nourah bint Abdulrahman University Researchers Supporting Project number (PNURSP2025R138), Princess Nourah bint Abdulrahman University, Riyadh, Saudi Arabia.

Funding

This study is supported via funding from Prince Sattam

bin Abdulaziz University project number (PSAU/2025/R/1447).

Princess Nourah bint Abdulrahman University Researchers Supporting Project number (PNURSP2025R138), Princess Nourah bint Abdulrahman University, Riyadh, Saudi Arabia.

References

Afshar, A., Jahandari, S., Rasekh, H., Shariati, M., Afshar, A. and Shokrgozar, A. (2020), "Corrosion resistance evaluation of rebars with various primers and coatings in concrete modified with different additives", *Constr. Build. Mater.*, **262**, p. 120034. https://doi.org/10.1016/j.conbuildmat.2020.120034

Arabnejad Khanouki, M.M., Ramli Sulong, N.H. and Shariati, M. (2010), "Investigation of seismic behaviour of composite structures with concrete filled square steel tubular (CFSST) column by push-over and time-history analyses", *Proceedings of the 4th International Conference on Steel Composite Structures*, pp. 21-23.

Arabnejad Khanouki, M.M., Ramli Sulong, N.H. and Shariati, M. (2011), "Behavior of through beam connections composed of CFSST columns and steel beams by finite element studying", *Adv. Mater. Res.*, **168**, 2329-2333. https://doi.org/10.4028/www.scientific.net/AMR.168-170.2329

Arani, K.S., Zandi, Y., Pham, B.T., Mu'azu, M.A., Katebi, J., Mohammadhassani, M., Khalafi, S., Mohamad, E.T., Wakil, K. and Khorami, M. (2019), "Computational optimized finite element modelling of mechanical interaction of concrete with fiber reinforced polymer", *Comput. Concrete, Int. J.*, **23**(1), 61-68. https://doi.org/10.12989/cac.2019.23.1.061

Armaghani, D.J., Mirzaei, F., Shariati, M., Trung, N.T., Shariati, M. and Trnavac, D. (2020), "Hybrid ANN-based techniques in predicting cohesion of sandy-soil combined with fiber", *Geomech. Eng., Int. J.*, **20**(3), 191-205. https://doi.org/10.12989/gae.2020.20.3.191

Aytaç, K. and Korçak, Ö. (2021), "IoT based intelligence for proactive waste management in Quick Service Restaurants", *J. Cleaner Product.*, **284**, p. 125401. https://doi.org/10.1016/j.jclepro.2020.125401

Bao, M., Yu, L. and Wang, Y. (1991), "Stress concentration structure with front beam for pressure sensor", *Sensors Actuators A: Phys.*, **28**(2), 105-112. https://doi.org/10.1016/0924-4247(91)85019-K

Benevenuta, S. and Fariselli, P. (2019), "On the upper bounds of the real-valued predictions", *Bioinform. Biol. Insights*, **13**, p. 1177932219871263. https://doi.org/10.1177/1177932219871263

Boaventura, A.C.C., Almeida, M.S.D.S., Costa, W.G.S., Pereira, Í.M.M., São Mateus, M.D.S.C., Brito, J.A. and Fiuza-Jr, R.A. (2024), "The influence of residual asphalt material in the mechanical behaviour of soil-RAP mixtures for use in paving", *Int. J. Pave. Eng.*, **25**(1), p. 2407901. https://doi.org/10.1080/10298436.2024.2407901

Cai, T., Zandi, Y., Agdas, A.S., Selmi, A., Issakhov, A. and Roco-Videla, A. (2021), "The compressive strength of concrete retrofitted with wind ash and steel slag pozzolans with a water-cement based polymers", *Adv. Concrete Constr., Int. J.*, **11**(6), 507-519. https://doi.org/10.12989/acc.2021.11.6.507

Cao, Y., Zandi, Y., Rahimi, A., Wu, Y., Fu, L., Wang, Q., Denić, N., Khadimallah, M.A., Milič, M. and Paunović, M. (2021), "A new intelligence fuzzy-based hybrid metaheuristic algorithm for analyzing the application of tea waste in concrete as natural fiber", *Comput. Electr. Agri.*, **190**, p. 106420. https://doi.org/10.1016/j.compag.2021.106420

Cao, Y., Chi, H., Zhu, Z., Fan, S., Zhang, Y., Tang, Y. and Hou, D. (2025), "Multi-Functional Self-Sensing Electronic Gasket for Structural Health Monitoring of Transportation Pipelines", *Adv. Funct. Mater.*, **35**(20), p. 2412634. https://doi.org/10.1002/adfm.202412634

Chahnasir, E.S., Zandi, Y., Shariati, M., Dehghani, E., Toghroli, A., Mohamad, E.T., Shariati, A., Safa, M., Wakil, K. and Khorami, M. (2018), "Application of support vector machine with firefly algorithm for investigation of the factors affecting the shear strength of angle shear connectors", *Smart Struct. Syst., Int. J.*, **22**(4), 413-424. https://doi.org/10.12989/sss.2018.22.4.413

Chen, C., Shi, L., Shariati, M., Toghroli, A., Mohamad, E.T., Bui, D.T. and Khorami, M. (2019), "Behavior of steel storage pallet racking connection-A review", *Steel Compos. Struct., Int. J.*, **30**(5), 457-469. https://doi.org/10.12989/scs.2019.30.5.457

Chen, X., Cui, J., Liu, Y., Zhang, X., Sun, J., Ai, R., Gu, W., Xu, J. and Lu, H. (2024), "Joint scene flow estimation and moving object segmentation on rotational LiDAR data", *IEEE Transact. Intell. Transport. Syst.*, **25**(11), 17733-17743. http://dx.doi.org/10.1109/TITS.2024.3432755

Chen, H., Zhu, D., Guo, Q., Zhao, F., Zhu, Y. and Yao, H. (2025), "Simulation, verification, and prediction of thermal response of bridgewire in electro-explosive device", *Measurement*, **253**, p. 117483. https://doi.org/10.1016/j.measurement.2025.117483

Cheng, S., Zhang, H., Chen, X., Wang, Y., Cheng, F., Sun, P., Li, Y., Yang, Z., Zhang, J., Sun, J. and Shao, J. (2025), "Electric-Assisted Coaxial Wet Spinning of Radially Oriented Boron Nitride Nanosheet-Based Composite Fiber with Highly Enhanced Piezoelectricity", *Adv. Fiber Mater.*, pp. 1-15. https://doi.org/10.1007/s42765-025-00567-0

Daie, M., Jalali, A., Suhatril, M., Shariati, M., Arabnejad Khanouki, M.M., Shariati, A. and Kazemi-Arbat, P. (2011), "A new finite element investigation on pre-bent steel strips as damper for vibration control", *Int. J. Phys. Sci.*, **6**(36), 8044-8050. https://doi.org/10.5897/IJPS11.1585

Dantzig, G.B. and Ramser, J.H. (1959), "The truck dispatching problem", *Manag. Sci.*, **6**(1), 80-91. https://doi.org/10.1287/mnsc.6.1.80

Davoodnabi, S.M. (2019), "Behavior of steel-concrete composite beam using angle shear connectors at fire condition", *Steel Compos. Struct., Int. J.*, **30**(2), 141-147. https://doi.org/10.12989/scs.2019.30.2.141

Davoodnabi, S.M., Mirhosseini, S.M. and Shariati, M. (2021), "Analyzing shear strength of steel-concrete composite beam with angle connectors at elevated temperature using finite element method", *Steel Compos. Struct., Int. J.*, **40**(6), 853-868. https://doi.org/10.12989/scs.2021.40.6.853

Ferrucci, F. and Bock, S. (2015), "A general approach for controlling vehicle en-route diversions in dynamic vehicle routing problems", *Transport. Res. Part B: Methodol.*, **77**, 76-87. https://doi.org/10.1016/j.trb.2015.03.003

Ghiani, G., Laporte, G. and Musmanno, R. (2022), *Introduction to Logistics Systems Management: With Microsoft Excel and Python Examples*, John Wiley & Sons.

Gong, B. and Li, H. (2024), "A couple Voronoi-RBSM modeling strategy for RC structures", *Struct. Eng. Mech., Int. J.*, **91**(3), 239-250. https://doi.org/10.12989/sem.2024.91.3.239

Hamidian, M., Shariati, M., Arabnejad, M.M.K. and Sinaei, H. (2011), "Assessment of high strength and light weight aggregate concrete properties using ultrasonic pulse velocity technique", *Int. J. Phys. Sci.*, **6**(22), 5261-5266. https://doi.org/10.5897/IJPS11.1081

Heydari, A. and Shariati, M. (2018), "Buckling analysis of tapered BDFGM nano-beam under variable axial compression resting on elastic medium", *Struct. Eng. Mech., Int. J.*, **66**(6), 737-748. https://doi.org/10.12989/sem.2018.66.6.737

Hosseinpour, E., Baharom, S., Badaruzzaman, W.H.W., Shariati, M. and Jalali, A. (2018), "Direct shear behavior of concrete filled hollow steel tube shear connector for slim-floor steel beams", *Steel Compos. Struct., Int. J.*, **26**(4), 485-499. http://dx.doi.org/10.12989/scs.2018.26.4.485

Hosur Shivaramaiah, N.K., Kattimani, S., Shariati, M. and Nguyen-Thoi, T. (2022), "Geometrically nonlinear behavior of two-directional functionally graded porous plates with four different materials", *Proceedings of the Institution of Mechanical Engineers, Part C: Journal of Mechanical Engineering Science*, **236**(22), 11008-11023. http://dx.doi.org/10.1177/09544062221111038

Hou, S., Zheng, Y., Zandi, Y., Khadimallah, M.A. and Ebtekar, A. (2022), "The free vibration analysis of carbon nanotubes-reinforced deep conical shells with an intermediate ring support under various boundary conditions", *Eng. Struct.*, **263**, p. 114291. https://doi.org/10.1016/j.engstruct.2022.114291

Hu, D., Liu, J., Li, Y. and Tan, Z. (2025a), "Prediction method of ground settlement for rectangular tunnel construction", *Tunnell. Undergr. Space Technol.*, **164**, p. 106814. https://doi.org/10.1016/j.tust.2025.106814

Hu, W., Chen, S., Liu, Z., Luo, X. and Xu, J. (2025b), "HA-RRT: A heuristic and adaptive RRT algorithm for ship path planning", *Ocean Eng.*, **316**, p. 119906. https://doi.org/10.1016/j.oceaneng.2024.119906

Hui, Y., Tang, Y., Yang, Q. and Mochida, A. (2024), "Numerical study on influence of surface vegetation on aerodynamics of high-rise buildings", *Sustain. Cities Soc.*, **107**, p. 105407. https://doi.org/10.1016/j.scs.2024.105407

Ismail, M., Shariati, M., Awal, A.A., Chiong, C.E., Chahnasir, E.S., Porbar, A., Heydari, A. and Khorami, M. (2018), "Strengthening of bolted shear joints in industrialized ferrocement construction", *Steel Compos. Struct., Int. J.*, **28**(6), 681-690. https://doi.org/10.12989/scs.2018.28.6.681

Jahandari, S., Tao, Z., Saberian, M., Shariati, M., Li, J., Abolhasani, M., Kazemi, M., Rahmani, A. and Rashidi, M. (2022), "Geotechnical properties of lime-geogrid improved clayey subgrade under various moisture conditions", *Road Mater. Pave. Des.*, **23**(9), 2057-2075. http://dx.doi.org/10.1080/14680629.2021.1950816

Jalali, A., Daie, M., Nazhadan, S.V.M., Kazemi-Arbat, P. and Shariati, M. (2012), "Seismic performance of structures with pre-bent strips as a damper", *Int. J. Phys. Sci.*, **7**(26), 4061-4072. https://doi.org/10.5897/IJPS11.1324

Jiang, T., Tang, Y., Xu, C. and Liu, W. (2025), "A calibration and error evaluation method of a combined tracking-based vision measurement system for meter-scale components", *IEEE Transact. Indust. Inform.*, **21**(6), 4958-4967. https://doi.org/10.1109/TII.2025.3547351

Katebi, J., Shoaei-parchin, M., Shariati, M., Trung, N.T. and Khorami, M. (2020), "Developed comparative analysis of metaheuristic optimization algorithms for optimal active control of structures", *Eng. Comput.*, **36**, 1539-1558. https://doi.org/10.1007/S00366-019-00780-7

Khanouki, M.A., Sulong, N.R., Shariati, M. and Tahir, M.M. (2016), "Investigation of through beam connection to concrete filled circular steel tube (CFCST) column", *J. Constr. Steel Res.*, **121**, 144-162. https://doi.org/10.1016/j.jcsr.2016.01.002

Khorami, M., Alvansazyazdi, M., Shariati, M., Zandi, Y., Jalali, A. and Tahir, M. (2017a), "Seismic performance evaluation of buckling restrained braced frames (BRBF) using incremental nonlinear dynamic analysis method (IDA)", *Earthq. Struct., Int. J.*, **13**(6), 531-538. https://doi.org/10.12989/eas.2017.13.6.531

Khorami, M., Khorami, M., Motahar, H., Alvansazyazdi, M., Shariati, M., Jalali, A. and Tahir, M.M. (2017b), "Evaluation of the seismic performance of special moment frames using incremental nonlinear dynamic analysis", *Struct. Eng. Mech., Int. J.*, **63**(2), 259-268. https://doi.org/10.12989/sem.2017.63.2.259

Khorramian, K., Maleki, S., Shariati, M., Jalali, A. and Tahir, M.M. (2017), "Numerical analysis of tilted angle shear connectors in steel-concrete composite systems", *Steel Compos. Struct., Int. J.*, **23**(1), 67-85. https://doi.org/10.12989/scs.2017.23.1.067

Li, D., Toghroli, A., Shariati, M., Sajedi, F., Bui, D.T., Kianmehr, P., Mohamad, E.T. and Khorami, M. (2019), "Application of polymer, silica-fume and crushed rubber in the production of Pervious concrete", *Smart Struct. Syst., Int. J.*, **23**(2), 207-214. https://doi.org/10.12989/sss.2019.23.2.207

Li, S., Liu, Q., Wang, E. and Wang, J. (2023), "Global quantitative understanding of non-equilibrium cell fate decision-making in response to pheromone", *iScience*, **26**(10), p. 107885. https://doi.org/10.1016/j.isci.2023.107885

Li, Y., Weng, X., Hu, D., Tan, Z. and Liu, J. (2025), "Data-Driven Method for Predicting Long-Term Underground Pipeline Settlement Induced by Rectangular Pipe Jacking Tunnel Construction", *J. Pipeline Syst. Eng. Practice*, **16**(3), p. 04025046. https://doi.org/10.1061/JPSEA2.PSENG-1855

Liang, R., Ding, W., Zandi, Y., Rahimi, A., Pourkhorshidi, S. and Khadimallah, M.A. (2022), "Buildings' internal heat gains prediction using artificial intelligence methods", *Energy Build.*, **258**, p. 111794. https://doi.org/10.1016/j.enbuild.2021.111794

Liu, K., Jiao, S., Nie, G., Ma, H., Gao, B., Sun, C., Xin, D., Saha, T.K. and Wu, G. (2024a), "On image transformation for partial discharge source identification in vehicle cable terminals of high-speed trains", *High Voltage*, **9**(5), 1090-1100. https://doi.org/10.1049/hve2.12487

Liu, Y., Li, X., Ge, L. and Zhang, Z. (2024b), "Ultralarge-area stitchless scanning probe lithography and in situ characterization system using a compliant nanomanipulator", *IEEE/ASME Transact. Mechatr.*, **29**(2), 924-935. https://doi.org/10.1109/TMECH.2023.3323385

Liu, Y., Li, X., Zhang, Y., Ge, L., Guan, Y. and Zhang, Z. (2024c), "Ultra-large scale stitchless AFM: advancing nanoscale characterization and manipulation with zero stitching error and high throughput", *Small*, **20**(1), p. 2303838. https://doi.org/10.1002/smll.202303838

Luo, Z., Sinaei, H., Ibrahim, Z., Shariati, M., Jumaat, Z., Wakil, K., Pham, B.T., Mohamad, E.T. and Khorami, M. (2019), "Computational and experimental analysis of beam to column joints reinforced with CFRP plates", *Steel Compos. Struct., Int. J.*, **30**(3), 271-280. https://doi.org/10.12989/scs.2019.30.3.271

Ma, K., Yu, Y., Yang, B. and Yang, J. (2019), "Demand-side energy management considering price oscillations for residential building heating and ventilation systems", *IEEE Transact. Indust. Inform.*, **15**(8), 4742-4752. https://doi.org/10.1109/TII.2019.2901306

Mehrabi, P., Wakil, K., Khorami, M., Shariati, M. and Safa, M. (2019), "Moment-rotation estimation of steel rack connection using extreme learning machine", *Steel Compos. Struct., Int. J.*, **31**(5), 427-435. http://dx.doi.org/10.12989/scs.2019.31.5.427

Mehrabi, P., Shariati, M., Kabirifar, K., Jarrah, M., Rasekh, H., Trung, N.T., Shariati, A. and Jahandari, S. (2021), "Effect of pumice powder and nano-clay on the strength and permeability of fiber-reinforced pervious concrete incorporating recycled concrete aggregate", *Constr. Build. Mater.*, **287**, p. 122652. https://doi.org/10.1016/j.conbuildmat.2021.122652

Milovančević, M., Marinović, J.S., Nikolić, J., Kitić, A., Shariati, M., Trung, N.T., Wakil, K. and Khorami, M. (2019), "UML diagrams for dynamical monitoring of rail vehicles", *Phys. A: Statist. Mech. Applicat.*, **531**, p. 121169. https://doi.org/10.1016/j.physa.2019.121169

Mohammadhassani, M., Nezamabadi-Pour, H., Suhatril, M. and Shariati, M. (2013a), "Identification of a suitable ANN

architecture in predicting strain in tie section of concrete deep beams", *Struct. Eng. Mech., Int. J.*, **46**(6), 853-868. https://doi.org/10.12989/sem.2013.46.6.853

Mohammadhassani, M., Suhatril, M., Shariati, M. and Ghanbari, F. (2013b), "Ductility and strength assessment of HSC beams with varying of tensile reinforcement ratios", *Struct. Eng. Mech., Int. J.*, **48**(6), 833-848. https://doi.org/10.12989/sem.2013.48.6.833

Mohammadhassani, M., Akib, S., Shariati, M., Suhatril, M. and Khanouki, M.A. (2014a), "An experimental study on the failure modes of high strength concrete beams with particular references to variation of the tensile reinforcement ratio", *Eng. Fail. Anal.*, **41**, 73-80. https://doi.org/10.1016/j.engfailanal.2013.08.014

Mohammadhassani, M., Nezamabadi-Pour, H., Suhatril, M. and Shariati, M. (2014b), "An evolutionary fuzzy modelling approach and comparison of different methods for shear strength prediction of high-strength concrete beams without stirrups", *Smart Struct. Syst., Int. J.*, **14**(5), 785-809. https://doi.org/10.12989/sss.2014.14.5.785

Naghipour, M., Niak, K.M., Shariati, M. and Toghroli, A. (2020a), "Effect of progressive shear punch of a foundation on a reinforced concrete building behavior", *Steel Compos. Struct., Int. J.*, **35**(2), 279-294. https://doi.org/10.12989/scs.2020.35.2.279

Naghipour, M., Yousofizinsaz, G. and Shariati, M. (2020b), "Experimental study on axial compressive behavior of welded built-up CFT stub columns made by cold-formed sections with different welding lines", *Steel Compos. Struct., Int. J.*, **34**(3), 347-359. https://doi.org/10.12989/scs.2020.34.3.347

Nasrollahi, S., Maleki, S., Shariati, M., Marto, A. and Khorami, M. (2018), "Investigation of pipe shear connectors using push out test", *Steel Compos. Struct., Int. J.*, **27**(5), 537-543. http://dx.doi.org/10.12989/scs.2018.27.5.537

Naveen Kumar, H.S., Kattimani, S., Marques, F.D., Nguyen-Thoi, T. and Shariati, M. (2023), "Geometrically nonlinear study of functionally graded saturated porous plates based on refined shear deformation plate theory and biot's theory", *Int. J. Struct. Stabil. Dyn.*, **23**(02), p. 2350013. http://dx.doi.org/10.1142/S021945542350013X

Nosrati, A., Zandi, Y., Shariati, M., Khademi, K., Aliabad, M.D., Marto, A., Mu'azu, M.A., Ghanbari, E., Mahdizadeh, M.B., Shariati, A. and Khorami, M. (2018), "Portland cement structure and its major oxides and fineness", *Smart Struct. Syst., Int. J.*, **22**(4), 425-432. https://doi.org/10.12989/sss.2018.22.4.425

Nouri, K., Sulong, N.R., Ibrahim, Z. and Shariati, M. (2021), "Behaviour of novel stiffened angle shear connectors at ambient and elevated temperatures", *Adv. Steel Constr.*, **17**(1), 28-38. https://doi.org/10.3390/su15010184

Paknahad, M., Shariati, M., Sedghi, Y., Bazzaz, M. and Khorami, M. (2018), "Shear capacity equation for channel shear connectors in steel-concrete composite beams", *Steel Compos. Struct., Int. J.*, **28**(4), 483-494. http://dx.doi.org/10.12989/scs.2018.28.4.483

Petković, B., Zandi, Y., Agdas, A.S., Nikolić, I., Denić, N., Kojić, N., Selmi, A., Issakhov, A., Milošević, S. and Khan, A. (2022), "Adaptive neuro fuzzy evaluation of energy and non-energy material productivity impact on sustainable development based on circular economy and gross domestic product", *Business Strat. Environ.*, **31**(1), 129-144. https://doi.org/10.1002/bse.2878

Qi, Z., Fei, Y., Chao, Z., Dong, Z. and Wang, H. (2026), "BLOTTER: Block-based lossless compression for highway structural health monitoring data", *Future Generat. Comput. Syst.*, p. 108003. https://doi.org/10.1016/j.future.2025.108003

Qian, Y., Liu, C., Yuan, Y., Xu, J., Wang, P. and Wang, K. (2025), "Numerical characterization and formation process study of rail light bands in high-speed turnout areas", *Eng. Fail. Anal.*, **168**, p. 109083. https://doi.org/10.1016/j.engfailanal.2024.109083

Razavian, L., Naghipour, M., Shariati, M. and Safa, M. (2020), "Experimental study of the behavior of composite timber columns confined with hollow rectangular steel sections under compression", *Struct. Eng. Mech., Int. J.*, **74**(1), 145-156. https://doi.org/10.12989/sem.2020.74.1.145

Sabetahd, R., Mousavi Ghasemi, S.A., Vafaei Poursorkhabi, R., Mohammadzadeh, A. and Zandi, Y. (2022), "Response Attenuation of a Structure Equipped with ATMD under Seismic Excitations Using Methods of Online Simple Adaptive Controller and Online Adaptive Type-2 Neural-Fuzzy Controller", *Computat. Intell. Neurosci.*, **2022**(1), p. 5832043. https://doi.org/10.1155/2022/5832043

Safa, M. and Kachitvichyanukul, V. (2019), "Moment rotation prediction of precast beam to column connections using extreme learning machine", *Struct. Eng. Mech., Int. J.*, **70**(5), 639-647. https://doi.org/10.12989/sem.2019.70.5.639

Safa, M., Shariati, M., Ibrahim, Z., Toghroli, A., Baharom, S.B., Nor, N.M. and Petković, D. (2016), "Potential of adaptive neuro fuzzy inference system for evaluating the factors affecting steel-concrete composite beam's shear strength", *Steel Compos. Struct., Int. J.*, **21**(3), 679-688. http://dx.doi.org/10.12989/scs.2016.21.3.679

Safa, M., Maleka, A., Arjomand, M.A., Khorami, M. and Shariati, M. (2019), "Strain rate effects on soil-geosynthetic interaction in fine-grained soil", *Geomech. Eng., Int. J.*, **19**(6), 533-542. https://doi.org/10.12989/gae.2019.19.6.533

Safa, M., Sari, P.A., Shariati, M., Suhatril, M., Trung, N.T., Wakil, K. and Khorami, M. (2020), "Development of neuro-fuzzy and neuro-bee predictive models for prediction of the safety factor of eco-protection slopes", *Phys. A: Statist. Mech. Applicat.*, **550**, p. 124046. https://doi.org/10.1016/j.physa.2019.124046

Sajedi, F. and Shariati, M. (2019), "Behavior study of NC and HSC RCCs confined by GRP casing and CFRP wrapping", *Steel Compos. Struct., Int. J.*, **30**(5), 417-432. https://doi.org/10.12989/scs.2019.30.5.417

Sedghi, Y., Zandi, Y., Shariati, M., Ahmadi, E., Azar, V.M., Toghroli, A., Safa, M., Mohamad, E.T., Khorami, M. and Wakil, K. (2018), "Application of ANFIS technique on performance of C and L shaped angle shear connectors", *Smart Struct. Syst., Int. J.*, **22**(3), 335-340. http://dx.doi.org/10.12989/sss.2018.22.3.335

Shaby, S.M., Premi, M.G. and Martin, B. (2015), "Enhancing the performance of mems piezoresistive pressure sensor using germanium nanowire", *Procedia Mater. Sci.*, **10**, 254-262. https://doi.org/10.1016/j.mspro.2015.06.048

Shah, S.N.R., Sulong, N.R., Shariati, M. and Jumaat, M.Z. (2015), "Steel rack connections: identification of most influential factors and a comparison of stiffness design methods", *PloS one*, **10**(10), p. e0139422. https://doi.org/10.1371/journal.pone.0139422

Shah, S.N.R., Sulong, N.R., Jumaat, M.Z. and Shariati, M. (2016a), "State-of-the-art review on the design and performance of steel pallet rack connections", *Eng. Fail. Anal.*, **66**, 240-258. https://doi.org/10.1016/j.engfailanal.2016.04.017

Shah, S.N.R., Sulong, N.R., Khan, R., Jumaat, M.Z. and Shariati, M. (2016b), "Behavior of industrial steel rack connections", *Mech. Syst. Signal Process.*, **70**, 725-740. https://doi.org/10.1016/j.ymssp.2015.08.026

Shah, S.N.R., Sulong, N.R., Shariati, M., Khan, R. and Jumaat, M.Z. (2016c), "Behavior of steel pallet rack beam-to-column connections at elevated temperatures", *Thin-Wall. Struct.*, **106**, 471-483. https://doi.org/10.1016/j.tws.2016.05.021

Shahabi, S., Sulong, N., Shariati, M. and Shah, S. (2016a), "Performance of shear connectors at elevated temperatures-A review", *Steel Compos. Struct., Int. J.*, **20**(1), 185-203. https://doi.org/10.12989/scs.2016.20.1.185

Shahabi, S., Sulong, N., Shariati, M., Mohammadhassani, M. and Shah, S.N.R. (2016b), "Numerical analysis of channel connectors under fire and a comparison of performance with different types of shear connectors subjected to fire", *Steel Compos. Struct.*, *Int. J.*, **20**(3), 651-669. https://doi.org/10.12989/scs.2016.20.3.651

Shahgoli, A.F., Zandi, Y., Heirati, A., Khorami, M., Mehrabi, P. and Petkovic, D. (2020), "Optimisation of propylene conversion response by neuro-fuzzy approach", *Int. J. Hydromechatr.*, **3**(3), 228-237. https://doi.org/10.1504/IJHM.2020.109918

Shariat, M., Shariati, M., Madadi, A. and Wakil, K. (2018), "Computational Lagrangian Multiplier Method by using for optimization and sensitivity analysis of rectangular reinforced concrete beams", *Steel Compos. Struct.*, *Int. J.*, **29**(2), 243-256. https://doi.org/10.12989/scs.2018.29.2.243

Shariati, M. (2008), "Assessment building using none-destructive test techniques (ultra sonic pulse velocity and Schmidt rebound hammer)", Doctoral Dissertation; Universiti Putra Malaysia.

Shariati, A. (2012), "Various types of shear connectors in composite structures: A review", *Int. J. Phys. Sci.*, **7**(22). http://dx.doi.org/10.18057/IJASC.2021.17.4.8

Shariati, M. (2013), "Behaviour of C-shaped shear connectors in stell concrete composite beams", Doctoral Dissertation; Jabatan Kejuruteraan Awam, Fakulti Kejuruteraan, Universiti Malaya.

Shariati, M., Ramli Sulong, N.H. and Arabnejad Khanouki, M.M. (2010), "Experimental and analytical study on channel shear connectors in light weight aggregate concrete", *Proceedings of the 4th International Conference on Steel Composite Structures*, pp. 21-23.

Shariati, M., Ramli-Sulong, N.H., Arabnejad, M.M., Shafigh, P. and Sinaei, H. (2011a), "Assessing the strength of reinforced concrete structures through Ultrasonic Pulse Velocity and Schmidt Rebound Hammer tests", *Scientif. Res. Essays*, **6**(1), 213-220. https://doi.org/10.5897/SRE10.879

Shariati, M., Ramli Sulong, N.H., Arabnejad Khanouki, M.M. and Shariati, A. (2011b), "Experimental and numerical investigations of channel shear connectors in high strength concrete", *Proceedings of the 2011 World Congress on Advances in Structural Engineering and Mechanics* (*ASEM'11+*).

Shariati, M., Ramli Sulong, N.H., Arabnejad, M.M.K.H. and Mahoutian, M. (2011c), "Shear resistance of channel shear connectors in plain, reinforced and lightweight concrete", *Scientif. Res. Essays*, **6**(4), 977-983. https://doi.org/10.5897/SRE10.1120

Shariati, M., Ramli Sulong, N.H., Sinaei, H., Arabnejad Khanouki, M.M. and Shafigh, P. (2011d), "Behavior of channel shear connectors in normal and light weight aggregate concrete (experimental and analytical study)", *Adv. Mater. Res.*, **168**. 2303-2307. https://doi.org/10.4028/www.scientific.net/AMR.168-170.2303

Shariati, A., Sulong, N.H., Suhatril, M. and Shariati, M. (2012a), "Investigation of channel shear connectors for composite concrete and steel T-beam", *Int. J. Phys. Sci.*, **7**(11), Article number: 0626DBF16390, pp. 11828-11831. http://dx.doi.org/10.5897/IJPS11.1604

Shariati, M., Ramli Sulong, N.H., Suhatril, M., Shariati, A., Arabnejad Khanouki, M.M. and Sinaei, H. (2012b), "Fatigue energy dissipation and failure analysis of channel shear connector embedded in the lightweight aggregate concrete in composite bridge girders", In: *Fifth International Conference on Engineering Failure Analysis*, pp. 1-4.

Shariati, M., Sulong, N.R. and Khanouki, M.A. (2012c), "Experimental assessment of channel shear connectors under monotonic and fully reversed cyclic loading in high strength concrete", *Mater. Des.*, **34**, 325-331. https://doi.org/10.1016/j.matdes.2011.08.008

Shariati, M., Sulong, N.R., Suhatril, M., Shariati, A., Khanouki, M.A. and Sinaei, H. (2012d), "Behaviour of C-shaped angle shear connectors under monotonic and fully reversed cyclic loading: An experimental study", *Mater. Des.*, **41**, 67-73. https://doi.org/10.1016/j.matdes.2012.04.039

Shariati, M., Sulong, N.R., Suhatril, M., Shariati, A., Khanouki, M.A. and Sinaei, H. (2013), "Comparison of behaviour between channel and angle shear connectors under monotonic and fully reversed cyclic loading", *Constr. Build. Mater.*, **38**, 582-593. https://doi.org/10.1016/j.conbuildmat.2012.07.050

Shariati, A., Shariati, M., Sulong, N.H.R., Suhatril, M. and Khanouki, M.M.A. (2014), "Experimental assessment of angle shear connectors under monotonic and fully reversed cyclic loading in high strength concrete", *Constr. Build. Mater.*, **52**, 276-283. https://doi.org/10.1016/j.conbuildmat.2013.11.037

Shariati, M., Ramli Sulong, N.H., Shariati, A. and Khanouki, M.A. (2016a), "Behavior of V-shaped angle shear connectors: experimental and parametric study", *Mater. Struct.*, **49**, 3909-3926. https://doi.org/10.1617/s11527-015-0762-8

Shariati, M., Sulong, N.R., Shariati, A. and Kueh, A.B.H. (2016b), "Comparative performance of channel and angle shear connectors in high strength concrete composites: An experimental study", *Constr. Build. Mater.*, **120**, 382-392. https://doi.org/10.1016/j.conbuildmat.2016.05.102

Shariati, M., Toghroli, A., Jalali, A. and Ibrahim, Z. (2017), "Assessment of stiffened angle shear connector under monotonic and fully reversed cyclic loading", *Proceedings of the 5th International Conference on Advances in Civil, Structural and Mechanical Engineering-CSM*.

Shariati, M., Tahir, M.M., Wee, T.C., Shah, S.N.R., Jalali, A., Abdullahi, M.A.M. and Khorami, M. (2018), "Experimental investigations on monotonic and cyclic behavior of steel pallet rack connections", *Eng. Fail. Anal.*, **85**, 149-166. https://doi.org/10.1016/j.engfailanal.2017.08.014

Shariati, M., Azar, S.M., Arjomand, M.A., Tehrani, H.S., Daei, M. and Safa, M. (2019a), "Comparison of dynamic behavior of shallow foundations based on pile and geosynthetic materials in fine-grained clayey soils", *Geomech. Eng., Int. J.*, **19**(6), 473-484. https://doi.org/10.12989/gae.2020.19.6.473

Shariati, M., Faegh, S.S., Mehrabi, P., Bahavarnia, S., Zandi, Y., Masoom, D.R., Toghroli, A., Trung, N.T. and Salih, M.N., (2019b), "Numerical study on the structural performance of corrugated low yield point steel plate shear walls with circular openings", *Steel Compos. Struct., Int. J.*, **33**(4), 569-581. https://doi.org/10.12989/scs.2019.33.4.569

Shariati, M., Heyrati, A., Zandi, Y., Laka, H., Toghroli, A., Kianmehr, P., Safa, M., Salih, M.N. and Poi-Ngian, S. (2019c), "Application of waste tire rubber aggregate in porous concrete", *Smart Struct. Syst., Int. J.*, **24**(4), 553-566. http://dx.doi.org/10.12989/sss.2019.24.4.553

Shariati, M., Mafipour, M.S., Mehrabi, P., Bahadori, A., Zandi, Y., Salih, M.N., Nguyen, H., Dou, J., Song, X. and Poi-Ngian, S. (2019d), "Application of a hybrid artificial neural network-particle swarm optimization (ANN-PSO) model in behavior prediction of channel shear connectors embedded in normal and high-strength concrete", *Appl. Sci.*, **9**(24), p. 5534. https://doi.org/10.3390/app9245534

Shariati, M., Mafipour, M.S., Mehrabi, P., Zandi, Y., Dehghani, D., Bahadori, A., Shariati, A., Trung, N.T., Salih, M.N. and Poi-Ngian, S. (2019e), "Application of Extreme Learning Machine (ELM) and Genetic Programming (GP) to design steel-concrete composite floor systems at elevated temperatures", *Steel Compos. Struct., Int. J.*, **33**(3), 319-332. https://doi.org/10.12989/scs.2019.33.3.319

Shariati, M., Rafie, S., Zandi, Y., Fooladvand, R., Gharehaghaj, B., Mehrabi, P., Shariat, A., Trung, N.T., Salih, M.N. and Poi-Ngian, S. (2019f), "Experimental investigation on the effect of

cementitious materials on fresh and mechanical properties of self-consolidating concrete", *Adv. Concrete Constr.*, *Int. J.*, **8**(3), 225-237. https://doi.org/10.12989/acc.2019.8.3.225

Shariati, M., Azar, S.M., Arjomand, M.A., Tehrani, H.S., Daei, M. and Safa, M. (2020a), "Evaluating the impacts of using piles and geosynthetics in reducing the settlement of fine-grained soils under static load", *Geomech. Eng.*, *Int. J.*, **20**(2), 87-101. https://doi.org/10.12989/gae.2020.20.2.087

Shariati, M., Ghorbani, M., Naghipour, M., Alinejad, N. and Toghroli, A. (2020b), "The effect of RBS connection on energy absorption in tall buildings with braced tube frame system", *Steel Compos. Struct.*, *Int. J.*, **34**(3), 393-407. https://doi.org/10.12989/scs.2020.34.3.393

Shariati, M., Grayeli, M., Shariati, A. and Naghipour, M. (2020c), "Performance of composite frame consisting of steel beams and concrete filled tubes under fire loading", *Steel Compos. Struct.*, *Int. J.*, **36**(5), 587-602. https://doi.org/10.12989/scs.2020.36.5.587

Shariati, M., Lagzian, M., Maleki, S., Shariati, A. and Trung, N.T. (2020d), "Evaluation of seismic performance factors for tension-only braced frames", *Steel Compos. Struct.*, *Int. J.*, **35**(4), 599-609. https://doi.org/10.12989/scs.2020.35.4.599

Shariati, M., Mafipour, M.S., Haido, J.H., Yousif, S.T., Toghroli, A., Trung, N.T. and Shariati, A. (2020e), "Identification of the most influencing parameters on the properties of corroded concrete beams using an Adaptive Neuro-Fuzzy Inference System (ANFIS)", *Steel Compos. Struct.*, *Int. J.*, **34**(1), 155-170. https://doi.org/10.12989/scs.2020.34.1.155

Shariati, M., Mafipour, M.S., Mehrabi, P., Ahmadi, M., Wakil, K., Trung, N.T. and Toghroli, A. (2020f), "Prediction of concrete strength in presence of furnace slag and fly ash using Hybrid ANN-GA (Artificial Neural Network-Genetic Algorithm)", *Smart Struct. Syst.*, *Int. J.*, **25**(2), 183-195. https://doi.org/10.12989/sss.2020.25.2.183

Shariati, M., Naghipour, M., Yousofizinsaz, G., Toghroli, A. and Tabarestani, N.P. (2020g), "Numerical study on the axial compressive behavior of built-up CFT columns considering different welding lines", *Steel Compos. Struct.*, *Int. J.*, **34**(3), 377-391. https://doi.org/10.12989/scs.2020.34.3.377

Shariati, M., Tahmasbi, F., Mehrabi, P., Bahadori, A. and Toghroli, A. (2020h), "Monotonic behavior of C and L shaped angle shear connectors within steel-concrete composite beams: an experimental investigation", *Steel Compos. Struct.*, *Int. J.*, **35**(2), 237-247. https://doi.org/10.12989/scs.2020.35.2.237

Shariati, M., Armaghani, D.J., Khandelwal, M., Zhou, J. and Khorami, M. (2021a), "Assessment of longstanding effects of fly ash and silica fume on the compressive strength of concrete using extreme learning machine and artificial neural network", *J. Adv. Eng. Computat.*, **5**(1), 50-74. http://dx.doi.org/10.25073/jaec.202151.308

Shariati, M., Davoodnabi, S.M., Toghroli, A., Kong, Z. and Shariati, A. (2021b), "Hybridization of metaheuristic algorithms with adaptive neuro-fuzzy inference system to predict load-slip behavior of angle shear connectors at elevated temperatures", *Compos. Struct.*, **278**, p. 114524. https://doi.org/10.1016/j.compstruct.2021.114524

Shariati, M., Mafipour, M.S., Mehrabi, P., Shariati, A., Toghroli, A., Trung, N.T. and Salih, M.N. (2021c), "A novel approach to predict shear strength of tilted angle connectors using artificial intelligence techniques", *Eng. Comput.*, **37**, 2089-2109. https://doi.org/10.1007/s00366-019-00930-x

Shariati, M., Mafipour, M.S., Mehrabi, P., Shariati, A., Toghroli, A. and Trung, N.T. (2021d), "A novel approach to predict shear strength of tilted angle connectors using artificial intelligence techniques", *Eng. Comput.*, **37**, 2089-2109. https://doi.org/10.1007/s00366-019-00930-x

Shariati, M., Mafipour, M.S., Ghahremani, B., Azarhomayun, F., Ahmadi, M., Trung, N.T. and Shariati, A. (2022), "A novel hybrid extreme learning machine–grey wolf optimizer (ELM-GWO) model to predict compressive strength of concrete with partial replacements for cement", *Eng. Comput.*, **38**(1), 757-779. https://doi.org/10.1007/s00366-020-01081-0

Shariati, M., Kamyab, H., Habibi, M., Ahmadi, S., Naghipour, M., Gorjinezhad, F., Mohammadirad, S. and Aminian, A. (2023), "Sulfuric acid resistance of concrete containing coal waste as a partial substitute for fine and coarse aggregates", *Fuel*, **348**, p. 128311. https://doi.org/10.1016/j.fuel.2023.128311

Shariati, M., Raeispour, M., Naghipour, M., Kamyab, H., Memarzadeh, A., Nematzadeh, M. and Toghroli, A. (2024), "Flexural behavior analysis of double honeycomb steel composite encased concrete beams: An integrated experimental and finite element study", *Case Stud. Constr. Mater.*, **20**, p. e03299. https://doi.org/10.1016/j.cscm.2024.e03299

Shi, H., Hayat, M. and Cai, J. (2024), "Unified open-vocabulary dense visual prediction", *IEEE Transact. Multimedia*, **26**, 8704-8716. https://doi.org/10.1109/TMM.2024.3381835

Sinaei, H., Jumaat, M.Z. and Shariati, M. (2011), "Numerical investigation on exterior reinforced concrete Beam-Column joint strengthened by composite fiber reinforced polymer (CFRP)", *Int. J. Phys. Sci.*, **6**(28), 6572-6579. https://doi.org/10.5897/IJPS11.1225

Sinaei, H., Shariati, M., Abna, A.H., Aghaei, M. and Shariati, A. (2012), "Evaluation of reinforced concrete beam behaviour using finite element analysis by ABAQUS", *Scientif. Res. Essays*, **7**(21), 2002-2009. https://doi.org/10.5897/SRE11.1393

Suhatril, M., Osman, N., Azura Sari, P., Shariati, M. and Marto, A. (2019), "Significance of surface eco-protection techniques for cohesive soils slope in Selangor, Malaysia", *Geotech. Geol. Eng.*, **37**, 2007-2014. https://link.springer.com/article/10.1007/s10706-018-0740-3

Sun, Y. and An, N. (2025), "Urban Public Space Design using Genetic Algorithm and Ant Colony Optimization", In: *2025 International Conference on Intelligent Systems and Computational Networks* (*ICISCN*), *IEEE*, pp. 1-5.

Sun, C. and Zhang, Y. (2024), "Research on the Reliability and Path Optimization of Three-Dimensional Warehousing Vehicles Based on Genetic-Ant Colony Algorithm", In: *2024 IEEE 2nd International Conference on Sensors*, *Electronics and Computer Engineering* (*ICSECE*), *IEEE*.

Taheri, E., Esgandarzadeh Fard, S., Zandi, Y. and Samali, B. (2021), "Experimental and numerical investigation of an innovative method for strengthening cold-formed steel profiles in bending throughout finite element modeling and application of neural network based on feature selection method", *Appl. Sci.*, **11**(11), p. 5242. https://doi.org/10.3390/app11115242

Tahmasbi, F., Maleki, S., Shariati, M., Ramli Sulong, N.H. and Tahir, M.M. (2016), "Shear capacity of C-shaped and L-shaped angle shear connectors", *PloS one*, **11**(8), p. e0156989. https://doi.org/10.1371/journal.pone.0156989

Tavakkoli, O., Kamyab, H., Shariati, M., Mohamed, A.M. and Junin, R. (2022), "Effect of nanoparticles on the performance of polymer/surfactant flooding for enhanced oil recovery: A review", *Fuel*, **312**, p. 122867. https://doi.org/10.1016/j.fuel.2021.122867

Toghroli, A., Mohammadhassani, M., Suhatril, M., Shariati, M. and Ibrahim, Z. (2014), "Prediction of shear capacity of channel shear connectors using the ANFIS model", *Steel Compos. Struct.*, *Int. J.*, **17**(5), 623-639. https://doi.org/10.12989/scs.2014.17.5.623

Toghroli, A., Shariati, M., Karim, M.R. and Ibrahim, Z. (2017), "Investigation on composite polymer and silica fume–rubber aggregate pervious concrete", *Proceedings of the 5th International Conference on Advances in Civil*, *Structural and Mechanical Engineering-CSM*.

Toghroli, A., Shariati, M., Sajedi, F., Ibrahim, Z., Koting, S., Mohamad, E.T. and Khorami, M. (2018a), "A review on pavement porous concrete using recycled waste materials", *Smart Struct. Syst.*, *Int. J.*, **22**(4), 433-440. https://doi.org/10.12989/sss.2018.22.4.433

Toghroli, A., Suhatril, M., Ibrahim, Z., Safa, M., Shariati, M. and Shamshirband, S. (2018b), "Potential of soft computing approach for evaluating the factors affecting the capacity of steel–concrete composite beam", *J. Intell. Manuf.*, **29**, 1793-1801. https://doi.org/10.1007/s10845-016-1217-y

Toghroli, A., Mehrabi, P., Shariati, M., Trung, N.T., Jahandari, S. and Rasekh, H. (2020), "Evaluating the use of recycled concrete aggregate and pozzolanic additives in fiber-reinforced pervious concrete with industrial and recycled fibers", *Constr. Build. Mater.*, **252**, p. 118997. https://doi.org/10.1016/j.conbuildmat.2020.118997

Trung, N.T., Alemi, N., Haido, J.H., Shariati, M., Baradaran, S. and Yousif, S.T. (2019), "Reduction of cement consumption by producing smart green concretes with natural zeolites", *Smart Struct. Syst.*, *Int. J.*, **24**(3), 415-425. http://dx.doi.org/10.12989/sss.2019.24.3.415

Vergara, D. (2025), "Voyage segmentation and propulsive power allocation: a data-driven approach for short sea shipping", In: *Chalmers Tekniska Hogskola*. https://doi.org/10.1016/j.joes.2023.11.002

Wang, H., Lang, X. and Mao, W. (2021a), "Voyage optimization combining genetic algorithm and dynamic programming for fuel/emissions reduction", *Transport. Res. Part D: Transport Environ.*, **90**, p. 102670. https://doi.org/10.1016/j.trd.2020.102670

Wang, H., Zandi, Y., Gholizadeh, M. and Issakhov, A. (2021b), "Buckling of porosity-dependent bi-directional FG nanotube using numerical method", *Adv. Nano Res.*, *Int. J.*, **10**(5), 493-507. https://doi.org/10.12989/anr.2021.10.5.493

Wang, L., Lv, Y., Wang, T., Wan, S. and Ye, Y. (2025a), "Assessment of the impacts of the life cycle of construction waste on human health: lessons from developing countries", *Engineering*, **32**(2), 1348-1369. https://doi.org/10.1108/ECAM-06-2023-0610

Wang, Y., Hui, Y., Chen, X., Zhao, D., Cheng, S., Zhu, R., Sun, L., Cui, Y., Sun, P., Gao, Y. and Zhang, J. (2025b), "Perforated piezoresistive film-based flexible bidirectional strain sensors for large bending deformation detection and health monitoring of glass fiber-reinforced polymers", *Compos. Part B: Eng.*, **293**, p. 112111. https://doi.org/10.1016/j.compositesb.2025.112111

Wang, Y., Wei, Y., Wei, Y., Zhen, L. and Deng, S. (2025c), "Collaborative multidepot split delivery network design with three-dimensional loading constraints", *Transport. Res. Part E: Logist. Transport. Rev.*, **196**, p. 104032. https://doi.org/10.1016/j.tre.2025.104032

Wei, X., Shariati, M., Zandi, Y., Pei, S., Jin, Z., Gharachurlu, S., Abdullahi, M.M., Tahir, M.M. and Khorami, M. (2018), "Distribution of shear force in perforated shear connectors", *Steel Compos. Struct.*, *Int. J.*, **27**(3), 389-399. https://doi.org/10.12989/scs.2018.27.3.389

Wei, Z., Zandi, Y., Gholizadeh, M., Selmi, A., Roco-Videla, A. and Konbr, U. (2021), "On the optimization of building energy, material, and economic management using soft computing", *Adv. Concrete Constr.*, *Int. J.*, **11**(6), 455-468. https://doi.org/10.12989/acc.2021.11.6.455

Xia, Z., Shu, J., Ding, W., Gao, Y., Duan, Y., Debono, C.J., Prakash, V., Seychell, D. and Borg, R.P. (2025), "Complete-coverage path planning for surface inspection of cable-stayed bridge tower based on building information models and climbing robots", *Comput.-Aided Civil Infrastr. Eng.* https://doi.org/10.1111/mice.13469

Xie, Q. (2019), "An experimental study on the effect of CFRP on behavior of reinforce concrete beam column connections", *Steel Compos. Struct.*, *Int. J.*, **30**(5), 433-441. https://doi.org/10.12989/scs.2019.30.5.433

Xie, B., Guo, Y., Chen, Y., Zhang, H., Xiao, J., Hou, M., Liu, H., Ma, L., Chen, X. and Wong, C. (2025), "Advances in graphene-based electrode for triboelectric nanogenerator", *Nano-Micro Lett.*, **17**(1), p. 17. https://doi.org/10.1007/s40820-024-01530-1

Yazdani, M., Kabirifar, K., Frimpong, B.E., Shariati, M., Mirmozaffari, M. and Boskabadi, A. (2021), "Improving construction and demolition waste collection service in an urban area using a simheuristic approach: A case study in Sydney, Australia", *J. Cleaner Product.*, **280**, p. 124138. https://doi.org/10.1016/j.jclepro.2020.124138

Yin, Q., Xin, T., Zhenggang, H. and Minghua, H. (2023), "Measurement and analysis of deformation of underlying tunnel induced by foundation pit excavation", *Adv. Civil Eng.*, **2023**(1), p. 8897139. https://doi.org/10.1155/2023/8897139

Yu, W., Shu, J., Yang, Z., Ding, H., Zeng, W. and Bai, Y. (2025), "Deep learning-based pipe segmentation and geometric reconstruction from poorly scanned point clouds using BIM-driven data alignment", *Automat. Constr.*, **173**, p. 106071. https://doi.org/10.1016/j.autcon.2025.106071

Zandi, Y., Burnaz, O. and Durmuş, A. (2012), "Determining the temperature distributions of fire exposed reinforced concrete cross-sections with different methods", *Res. J. Environ. Earth Sci.*, **4**(8), 782-788. https://doi.org/10.1002/fam.2317

Zandi, Y., Marto, A., Wei, X., Karaca, Z., Dao, D.K., Toghroli, A., Hashemi, M.H., Sedghi, Y., Wakil, K. and Khorami, M. (2018), "Computational investigation of the comparative analysis of cylindrical barns subjected to earthquake", *Steel Compos. Struct.*, *Int. J.*, **28**(4), 439-447. https://doi.org/10.12989/scs.2018.28.4.439

Zhang, C., Zhang, D., Zhang, M., Zhang, J. and Mao, W. (2022a), "A three-dimensional ant colony algorithm for multi-objective ice routing of a ship in the Arctic area", *Ocean Eng.*, **266**, p. 113241. https://doi.org/10.1016/j.oceaneng.2022.113241

Zhang, Y., Deng, X. and Zhang, Y. (2022b), "Generation of sub-item load profiles for public buildings based on the conditional generative adversarial network and moving average method", *Energy Build.*, **268**, p. 112185. https://doi.org/10.1016/j.enbuild.2022.112185

Ziaei-Nia, A., Shariati, M. and Salehabadi, E. (2018), "Dynamic mix design optimization of high-performance concrete", *Steel Compos. Struct.*, *Int. J.*, **29**(1), 67-75. https://doi.org/10.12989/scs.2018.29.1.067